Acta Astronautica 214 (2024) 722–736

Contents lists available at ScienceDirect

Acta Astronautica

journal homepage: www.elsevier.com/locate/actaastro

Research Paper

Development and standalone testing of the Air-breathing Microwave Plasma CAThode (AMPCAT)

Mansur Tisaev [a,*], Burak Karadag [a], Eugenio Ferrato [b,1], Tommaso Andreussi [b,1], Andrea Lucca Fabris [a]

[a] Surrey Space Centre, University of Surrey, Guildford, GU2 7XH, UK
[b] Institute of Mechanical Intelligence, Scuola Superiore Sant'Anna, Pisa, 56010, Italy

ARTICLE INFO

Keywords:
Air-breathing electric propulsion
VLEO
AETHER
Microwave cathode neutraliser
AMPCAT

ABSTRACT

Air-breathing electric propulsion (ABEP) refers to a spacecraft in very-low Earth orbit (VLEO) harnessing upper atmospheric air as propellant for an electric thruster. This allows the orbital altitude to be maintained via drag-compensation, removing the need for on-board propellant storage and allowing a mission lifetime which is not limited by propellant capacity. A cathode (or neutraliser) is required for the high-specific impulse electrostatic thruster designs proposed for an ABEP application. One such study is the AETHER EU H2020 project, which aims to design an ABEP system that can be tested on-ground in a VLEO-representative environment. There is therefore a need to develop a cathode for ABEP as conventional thermionic hollow cathodes are susceptible to oxygen poisoning. The Air-breathing Microwave Plasma CAThode (AMPCAT) presented here is based on a plasma electron source, using a 2.45 GHz microwave antenna directly-inserted into the plasma volume to ionise neutral air particles. This study details the cathode design and the results of iterative standalone testing, with a particular focus on: (a) the identification of a dual-mode current emission, with transition from lower- to higher-current mode with air at bias values around 70 V between the extracting anode and internal cathode surfaces, (b) a comparison of performance relative to xenon, for which the peak extracted current is 30–40% higher than air at equivalent inputs, and (c) the effect of antenna electrical isolation, using alumina shielding thicknesses in the 0.1–0.7 mm range. Standalone cathode tests demonstrate 0.8 A of stable extracted current with 0.1 mg/s mass flow rate of a $0.48O_2 + 0.52N_2$ mixture, relative bias of 80 V and input microwave power of 70 W. To the authors' knowledge, the demonstration of an extracted current in the 1 A order using air, without visible material degradation after several hours of operation, is a novel development in the cathode literature.

1. Introduction

The air-breathing electric propulsion (ABEP) concept involves a spacecraft which passes through the residual atmosphere in very-low Earth orbit (VLEO), broadly defined as altitudes below 400 km. The onset, rarefied air is collected and used as propellant for an electric thruster, with the thrust produced compensating the atmospheric drag experienced by the spacecraft. As a result, a spacecraft with an ABEP system that is capable of full drag compensation does not require onboard propellant storage and is able to operate in the VLEO altitude range with a mission lifetime that is not limited by propellant capacity [1].

Previous missions in VLEO include the European Space Agency's (ESA) GOCE spacecraft [2] and the SLATS mission of the Japan Aerospace Exploration Agency (JAXA) [3]. Both GOCE and SLATS used conventional electric propulsion systems with onboard xenon propellant to orbit at average altitude ranges of 260–230 km and 270–180 km respectively, until propellant depletion. Re-entry occurs rapidly once onboard propellant is exhausted for a conventional thruster, for instance a 200 kg spacecraft in an approximately circular orbit at 200 km altitude is expected to re-enter after around 15 days without propulsion [4].

The ability to operate a long-duration mission in VLEO using ABEP is advantageous for several types of spacecraft, such as: (a) an increased image resolution at a given aperture size for Earth observation missions, (b) access to measuring atmospheric, magnetic, radiation and gravitational properties in a scarcely-sampled altitude range for science missions, and (c) a low-latency connection to ground-based users for telecommunications satellites [1]. The ABEP concept is also applicable

* Corresponding author.
E-mail address: m.tisaev@surrey.ac.uk (M. Tisaev).
[1] Former affiliation: SITAEL S.p.A., Pisa, 56121, Italy.

https://doi.org/10.1016/j.actaastro.2023.11.028
Received 21 July 2023; Received in revised form 31 October 2023; Accepted 19 November 2023
Available online 24 November 2023

for other bodies in our solar system with an atmosphere, for instance Mars [5].

Aspects of the design for an air-breathing thruster system have been presented by several previous studies, such as [5–9]. A recent review of the literature is provided in [10]. The most common configuration comprises a passive intake, which collects and compresses the onset airflow via the high relative (orbital) speed of around 7.8 km/s, coupled to an electric thruster, which ionises and accelerates air particles to produce a thrust for preventing the orbital decay due to atmospheric drag. Power generation for the thruster and other spacecraft subsystems is typically assumed to be provided by solar arrays. Recent studies investigating the required thruster performance for an ABEP system to achieve drag-compensation have found that a high thruster specific impulse (I_{sp}) is key, with a minimum I_{sp} of around 3000 s needed [4, 11–13]. This predominantly originates from the significant level of tangential drag produced by spacecraft surfaces in the free-molecular regime, even if the spacecraft and arrays are aligned with the VLEO air flow. These results suggest that electrostatic thruster designs, which require a cathode and typically demonstrate high I_{sp} values, are good candidates for an ABEP system. The development of a thruster system using electrostatic ion acceleration is the aim of the AETHER (Air-breathing Electric THrustER) EU H2020 research project, which brings together industrial and academic partners from across Europe to design an ABEP system capable of achieving drag compensation and of being tested in a VLEO-representative environment on-ground [11,14].

A cathode (or neutraliser) is a key component of electrostatic thruster systems, such as the Gridded-Ion Thruster (GIT) and Hall-Effect Thruster (HET) classes that have the most heritage in the electric propulsion field [15, p. 243], in which the cathode typically: (a) provides primary electrons for sustaining ionisation, (b) forms the negative electrode of the potential profile for electrostatic ion acceleration, and (c) supplies the neutralisation current to balance the positive charge of the thruster ion beam. The AETHER thruster design proposes successive ionisation and acceleration stages, with exploration of both GIT- and HET-based approaches for the acceleration mechanism [11]. A cathode capable of operating on air is therefore a necessary component of the AETHER system and forms the University of Surrey's contribution to the project's hardware development. The AETHER project introduces targets for the cathode performance based on approximate platform specifications and an intended dawn-dusk Sun-Synchronous Orbit (SSO) at an altitude range of 190–240 km. For instance, the reference air composition is $0.48O + 0.52N_2$, the expected (post-intake) air mass flow rate available to the cathode is 0.04–0.1 mg/s and the inlet cathode particle density is in the range of $0.5–5 \times 10^{18}$ m^{-3}. It should be noted that these values are targets and contain a significant margin for flexibility, given the general novelty of air-breathing cathode technology.

Neutralisers for electric propulsion are most commonly based on the hollow cathode design, typically capable of a high current density at low input power (for instance 10 A/cm^2 in the 100 W order [15, p. 245]) via thermionic electron emission from the surface of low work function material such as barium-oxide impregnated tungsten (BaO-W) or lanthanum-hexaboride (LaB6). However, these cathodes undergo poisoning of the emitter surface with exposure to oxygen, prompting a significant decrease in the current density at even minimal values of air pressure ($\sim 10^{-3}$ mbar) [16,17]. Hollow cathodes are therefore not applicable as a neutraliser for a fully air-breathing propulsion system, in which the cathode operates on a subset of the total intake flow, composed almost entirely of oxygen and nitrogen. This is demonstrated by tests of a LaB6 hollow cathode with a $0.48O_2 + 0.52N_2$ propellant fraction of up to 12% (xenon balance), resulting in sparking in the cathode plume and significant erosion of internal cathode components within the short test duration [11].

C12A7:2e- electride has been suggested in the literature as an alternative emitter material to replace BaO-W and LaB6 due to a lower work function, which should allow a reduced operating temperature and increased resistance to poisoning with air. However, the most recent studies report difficulty with using C12A7:2e- as a cathode material, for instance requiring excessively high propellant flow rates [18] or due to the proximity of the temperature required for current emission and the melting point of the material itself [19]. The possibility of operation with air therefore remains some way from being investigated. Based on these factors, a plasma electron source is chosen as the approach for this study, since an alternative to a hollow cathode is required that remains capable of a current in the 1 A order of magnitude.

Plasma electron source cathodes ionise neutral propellant particles to sustain a plasma discharge, with positive ions collected on internal surfaces charged to a negative relative bias and, via the conservation of charge quasi-neutrality, electrons extracted out of the cathode along a positive potential gradient. The positive bias is generally provided by the thruster ion beam. However, if testing the cathode in a standalone configuration, a positively-biased plate is positioned downstream of the extraction orifice to act as the anode of the system. Before comparing the performance of different plasma cathode types presented in the literature, it is useful to define two metrics to represent the efficiency of cathode operation. These are the power efficacy C_e and the utilisation factor U_i:

$$C_e = \frac{I_{extr}}{P_{tot}} = \frac{I_{extr}}{P_D + P_{in}} \qquad U_i = \frac{I_{extr}}{I_A} = \frac{I_{extr} M}{e\dot{m}} \tag{1}$$

where M is the ion mass in kg, e is the electron charge, $\dot{m}$ is the mass flow rate of neutral propellant in kg/s and P_{tot} is the total cathode power. This is the sum of the discharge power $P_D = I_{extr}|V_b|$ required to generate the extracted current at a given bias V_b, and any additional cathode power P_{in}. C_e represents the emission current per unit of required cathode power. It is typically expressed in mA/W and also often given as the inverse C_e^{-1}, representing the current power cost in W/A. U_i denotes the emission current that can be extracted per unit of equivalent current expected from the propellant mass flow rate, assuming each inlet particle undergoes a single ionisation. U_i is therefore useful as a measure of how effectively propellant is ionised in the cathode. High values of both C_e and U_i are desirable, meaning a large current can be extracted from low cathode power and propellant mass flow rate.

Looking at the plasma cathode literature, a DC-discharge neutraliser motivated by the HET operating principle is investigated in [20], whereby ionisation is based on electron acceleration due to the cross-product of the static electric and magnetic (B) fields, commonly referred to as the $E \times B$ drift. The performance demonstrated from testing a range of conventional and alternative propellants (xenon, krypton, argon, helium, water and air) is low relative to other alternative neutralisers, with a peak current of 0.24 A and minimum C_e^{-1} of 290 W/A. However, air demonstrates the second lowest power cost behind argon and the highest U_i. This suggests that a DC-based ionisation process can be relatively effective for operation of a plasma neutraliser with air. Radio-frequency (RF) is also investigated as an ionisation source for plasma cathodes, such as the study presented in [21]. This demonstrates a maximum extracted current of 3.3 A with xenon at a power cost of around 100 W/A and utilisation factor of 15, based on power deposition into the Inductively-Coupled Plasma (ICP) from a helical RF coil. The authors also demonstrate coupling of the RF cathode with a Hall-effect-type thruster in comparison to a hollow cathode, obtaining matching discharge current, thrust and anode efficiency values [22]. As well as this, the development of RF cathodes has been discussed in multiple studies, such as those of [23–26].

A frequency in the microwave-range is also commonly used in plasma cathode literature, typically operating in the 2–5 GHz range. The work of [27,28] investigates the use of both: (a) a coaxial line with an antenna directly inserted into the plasma, and (b) a waveguide input into the cathode cavity, as the method of feeding microwave power into the plasma. The plasma-interfacing antenna configuration demonstrates higher extracted current values, with a maximum of 2.6

A recorded with xenon, yielding $C_e^{-1} = 98$ W/A and utilisation factor of $U_i = 12$. A particularly mature microwave cathode is the μ10 neutraliser developed by JAXA [29–31], and flown on the Hayabusa-1 and 2 asteroid sample return missions. The neutraliser design has undergone a number of studies which include endurance testing for 48000 hours demonstrated on-ground and > 6500 hours in space [32]. The μ10 neutraliser operates at a nominal current of 0.18 A, allowing the use of relatively low values for total bias voltage and microwave power of 32 V and 8 W respectively [31]. This corresponds with a power cost of $C_e^{-1} = 76$ W/A and utilisation factor of $U_i = 3.6$ with xenon. Versions of the neutraliser are coupled to both GIT and HET-type thruster designs, showing comparable emission current to standalone tests [33,34]. As a summary, the key performance metrics of the cathodes referred to in this section are presented as part of Table 6.

Based on the preceding literature review, this study considers a plasma cathode design which operates in the microwave frequency range and uses an antenna directly inserted into the plasma volume. This is primarily motivated by: (a) literature studies showing an extracted current in the desired 1 A order of magnitude achievable with xenon for this type of cathode, (b) high efficiencies for power- and propellant-usage reported in literature at the low power and flow rate values intended for the AETHER neutraliser, and (c) more compact microwave components than equivalents for RF due to smaller wavelengths associated with the higher microwave frequency range, e.g. components based on a $\lambda/4$ scale factor. The development of the cathode in this study, titled the Air-breathing Microwave Plasma CAThode (AMPCAT), is pursued through the iterative design of a series of prototypes based on standalone testing. To the authors' best knowledge, this is the first cathode developed and tested to operate with air as propellant, demonstrating an extracted current in the 1 A order of magnitude. The remainder of this article is organised as follows. Section 2 presents the prototype design and test setup, before the dual-current mode behaviour and effect of varying internal surface bias is detailed in Section 3. The antenna sputtering and deposition on cathode surfaces with the exposed antenna design is analysed in Section 4, which introduces and investigates electrical isolation of the antenna. Section 5 presents a comparison of standalone extracted current performance between air and xenon. Lastly, the evolution of the AMPCAT prototype design and continuous operation with air are detailed in Section 6.

2. Microwave cathode design

2.1. Operating principle

In the cathode, propellant is fed into the internal volume surrounding a microwave antenna. Ionisation of the neutral particles occurs through energy transfer resulting from the time-varying electric (E) and magnetic (B) fields emitted by the antenna, which supports a plasma discharge within the cathode. An ion current I_i is collected from the plasma on the conducting internal cathode surfaces due to a negative applied bias and this allows for an equal electron current I_{extr} to be extracted, while maintaining charge conservation in the plasma. This electron current is driven by a positive potential gradient through the cathode orifice resulting from the positive potential of the thruster ion beam. In standalone testing, the thruster potential is simulated by a positively-biased extracting anode positioned downstream of the cathode orifice. The total relative bias between the plasma-interfacing cathode surfaces and the extracting anode is termed V_b.

Ion-collection occurs via a Child-Langmuir sheath at the internal cathode walls, since the negative bias imposes a large potential drop through the sheath relative to the electron temperature T_e (in eV) of the bulk plasma. The ion current collected $I_i = J_i A_i$, where J_i is the ion-current density and A_i the ion-collecting area of the conducting surfaces exposed to the plasma. The current density is found as:

$$J_i = n_i e v = n_i e \sqrt{\frac{2e(\phi_0 - \phi)}{M}} = \frac{4\varepsilon_0}{9}\sqrt{\frac{2e}{M}}\frac{V^{3/2}}{d^2} \tag{2}$$

where n_i is the ion density in the plasma, e is the electron charge, v is the ion velocity at the wall, $\phi_0 - \phi = V$ is the potential drop through the sheath and d is the thickness of the sheath. The ion density is typically assumed as approximately equal to the electron density n_e in the bulk plasma based on charge quasi-neutrality.

Microwaves must penetrate into the plasma in order for ionisation to occur, however this wave-transmission is limited by the plasma frequency ω_p. This value is based on n_e, therefore defining a maximum cut-off plasma (electron) density n_c for which a given wave frequency f is able to pass through the plasma. Above this density, wherein the plasma is overdense, an incoming wave is reflected at the plasma surface and becomes evanescent, thus unable to propagate through the bulk plasma. This criteria is found via:

$$\omega_p = \sqrt{\frac{n_e e^2}{m\varepsilon_0}} \quad \longrightarrow \quad n_c = \frac{m\varepsilon_0(2\pi f)^2}{e^2} \tag{3}$$

where ε_0 is the vacuum permittivity and m is the electron mass. For a microwave frequency $f = 2.45$ GHz, this defines a cut-off density $n_c = 7.4 \times 10^{16}$ m^{-3}. However, literature studies of plasma cathodes utilising a microwave antenna directly-inserted into the plasma volume consistently observe an overdense bulk plasma in the cathode [27,29]. This is due to direct heating of electrons by the time-varying E and B microwave fields in the immediate vicinity of the antenna. The extent of this region around the antenna is approximated by the plasma skin depth δ:

$$\delta = \frac{c}{\sqrt{\omega_p^2 - (2\pi f)^2}} \tag{4}$$

where c is the speed of light. For instance, a value of $n_e = 10^{18}$ m^{-3}, as observed for microwave cathodes in literature, estimates a thickness of $\delta = 5.5$ mm around the 2.45 GHz antenna in which microwave-electron energy transfer primarily occurs. Electrons in the antenna vicinity form an effective virtual-cathode, which supports efficient coupling of microwave energy into the plasma. Since microwaves do not penetrate extensively in the overdense regime, electron-neutral collisions are expected to form the principal ionisation mechanism, based on diffusion of high-energy electrons from the antenna near-field into a neutral population with density n_n. It should be noted that negative ion production can occur in air plasma due to the electronegative nature of oxygen, unlike xenon which only forms positive ions. For instance, negative oxygen ions can form through dissociative electron-attachment reactions with oxygen neutrals (e.g. $e^- + O_2 \rightarrow O^- + O$) [35]. As a result, a fraction of the negative current extracted from the cathode may be composed of negative oxygen ions in the case of air. However, it is expected that this fraction is small since collisions between electrons and neutral air species are significantly more likely to result in ionisation events that form positive ions in a stable (non-pulsed) plasma discharge. For instance, simulations in [36] find a higher reaction rate for positive rather than negative oxygen ion production for $T_e >$ 3 eV and a positive ion production rate $\sim 10^2$ larger at $T_e = 10$ eV, which is realistic for the higher-density plasma which supports oxygen ionisation primarily in the antenna vicinity (see Section 3.1). While the low relative likelihood of negative oxygen ion production and the electron extraction mechanisms observed for conventional propellants in the plasma cathode literature suggest that the extracted current is primarily composed of electrons, it is anticipated that further testing as part of future work will quantify the ratio of electrons to negative ions in the extracted AMPCAT current.

2.2. Initial prototype design

The design of early cathode prototypes in this study is intended to exploit electron cyclotron resonance (ECR) for efficient electron-heating, as detailed previously in [37]. Testing observes an extracted current with xenon which correlates well with primarily ECR-based

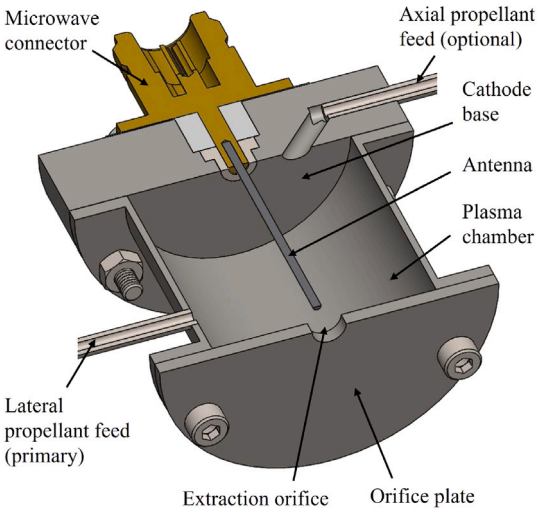

Fig. 1. Cross-section of initial cathode prototype design.

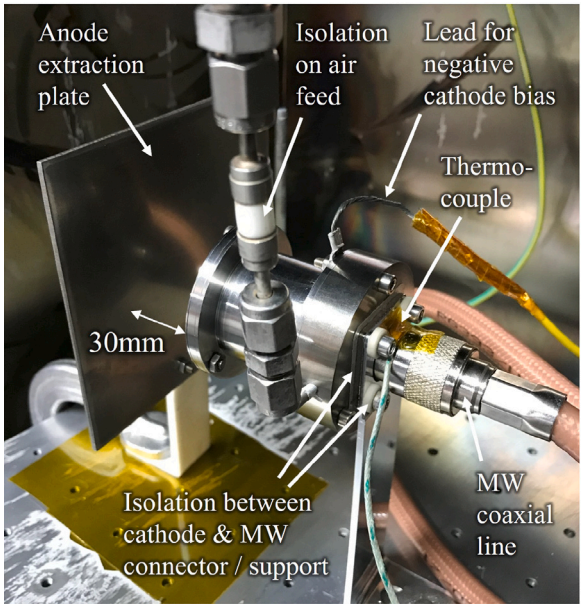

Fig. 2. Standalone test setup within vacuum chamber.

electron-heating, similarly to other literature [28,29]. However, there is a significant difference with air, for which the presence of an applied magnetic-field only serves to suppress the extracted current (I_{extr}), and these results are presented in [38].

This early experience motivates the design aspects of the initial prototype considered in this study, which is shown in Fig. 1. There is no magnetic-field applied to the cathode volume since $B = 0$ yields an increased electron current with air, as well as significantly simplifying the prototype design and assembly. The plasma-interfacing surfaces are machined from grade 304 stainless steel, chosen due to: (a) good conductivity for ion-collection (2.4% copper conductivity [39]), and (b) good resistance to oxidation at the elevated temperatures (up to $\sim$ 200 °C) expected under plasma exposure. The cathode internal surfaces are composed of the cathode base, plasma chamber and orifice plate (interior side), which together form the ion collection region as shown in Fig. 1. A 2.45 GHz antenna manufactured from 1.25 mm diameter molybdenum wire extends along the central cathode axis, with an efficient $\lambda/4$ radiating length to maximise the magnitude of radiated E-field [40, p. 200]. The antenna interfaces with an N-type commercial connector, which links to a coaxial microwave line. PTFE and alumina sleeve components isolate the central microwave pin from the cathode housing, ensuring that the effective coaxial line is extended up to the plasma volume. Since the internal surfaces, and thus all the stainless steel body, is negatively-biased, the grounded outer conductor of the microwave connector is isolated at its interface using a 0.2 mm thick Mica gasket. Propellant is input into the chamber via a lateral or axial inlet connected to 1/8″ grade 316 stainless steel tubing, with both inlets designed to impinge on the antenna. Tests recording the internal neutral pressure for an early prototype show an equivalent global neutral density inside the cathode regardless of the inlet position. This is verified for the initial prototype described here by means of an equal extracted current observed for switching between the radial or axial propellant input. As a result, the lateral inlet is used for all subsequent tests.

The internal AMPCAT diameter of $D_{in} = 33$ mm is based on supporting a neutral density of 5×10^{18} m^{-3} in the cathode channel (no orifice) at the nominal air mass flow rate of $\dot{m} = 0.1$ mg/s, estimated for the case of a fully-representative air-breathing platform in which the cathode is fed by the post-intake flow. In the cathode prototype tested, electron current is extracted through an orifice located downstream of the antenna. A 5 mm diameter orifice is nominally used, as in Fig. 1, for which the internal neutral density is calculated as $n_n = 1.1\times10^{21}$ m^{-3} at the nominal $\dot{m} = 0.1$ mg/s flow rate of the $0.48O_2 + 0.52N_2$ mixture. These calculations are validated using a micro-Pirani pressure sensor for the case without plasma, leading to a percentage difference of 13 %. It is acknowledged that the nominal neutral density is several orders of magnitude higher than the ideal air-breathing target, however it is low compared to other plasma cathode literature [21,28]. The free-molecular flow calculations and pressure measurement of the neutral density values above are fully detailed in [38], which also presents investigations towards low-density operation with air.

2.3. Test setup

The configuration for standalone cathode testing is shown inside the vacuum chamber in Fig. 2. A grade 304 stainless steel plate is used as the extracting anode and is positioned 30 mm downstream of the cathode orifice. The anode is biased to +20 V in order to reproduce the approximate electric potential of the thruster plume [15, p. 338]. A negative DC bias is applied to the cathode body as shown in Fig. 2, requiring electrical isolation of components interfacing with the grounded chamber walls. This can be seen between the cathode and both the Brass microwave connector (outer conductor) and aluminium support bracket, using a Mica gasket at the cathode-connector interface and alumina bushes around the bracket fasteners. The propellant feed-line is similarly isolated upstream of the cathode using a ceramic spacer. A K-type thermo-couple is used to measure the cathode temperature. As seen in Fig. 2, it is typically fixed in the most temperature-critical position at the microwave connector to ensure that a dielectric-damaging temperature is not exceeded during tests. This is further detailed in Section 6.

A schematic of the test setup and equipment, both inside and outside the vacuum chamber, is shown in Fig. 3. Microwave power is supplied via a coaxial N-type line from a 2.45 GHz generator (Kuhne KUSG2.45-250A, forward power up to 250 W), which also displays the forward and reflected power. A stub tuner (Arios, max power 200 W) is used for impedance-matching along the microwave line to minimise the reflected power, usually reduced to below 1 W, and a DC block (MECA) isolates the line from any DC plasma current collected by the antenna. Small openings are drilled in the N-type microwave connectors within the vacuum chamber, to prevent non-evacuated air inside the connectors and the possibility of connector damage from a multi-pactor breakdown. The extracted current is recorded on the anode DC power supply (Sorensen DLM300-2, max 600 W, 300 V)

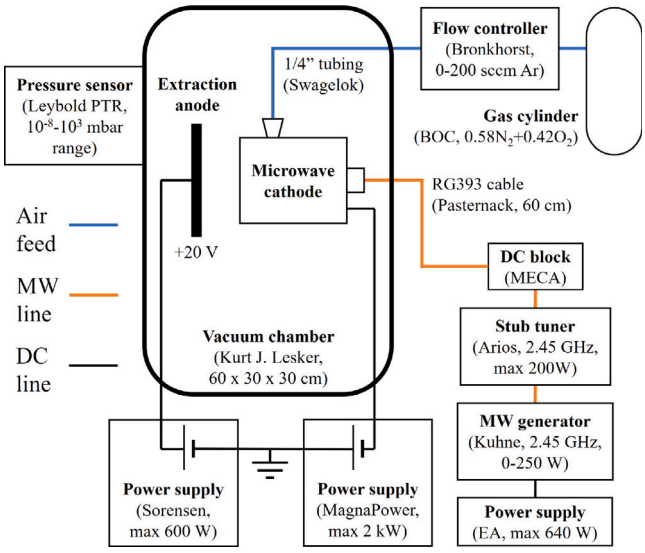

Fig. 3. Schematic of test setup and equipment.

Table 1
Test matrix for standalone characterisation tests.

Input	Start	End	Step
Cathode negative bias (V)	−20	−100	20
Microwave source power (W)	30	90	30
Air mass flow rate (mg/s)	0.05	0.15	0.05

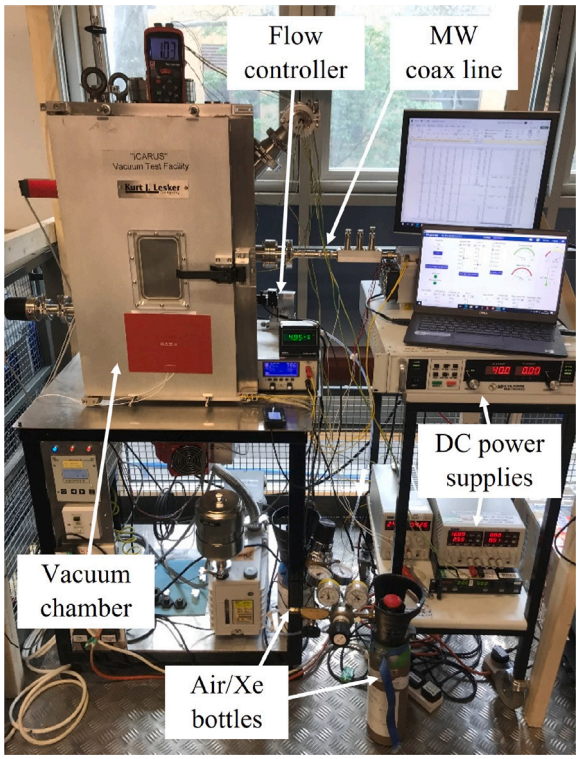

Fig. 4. Vacuum chamber apparatus for standalone tests.

as the time-averaged value. The collected ion-current is displayed on the cathode DC power supply (MagnaPower, max 2 kW at up to 12 A), and it is verified that these two values agree to within the 10 mA resolution of both power supplies in nominal cathode operation. Propellant is supplied from compressed gas bottles via a mass flow controller for both the $0.48O_2$ + $0.52N_2$ air mixture (Bronkhorst El-Flow, max 200 sccm Ar, precision 0.1 sccm) and xenon (Bronkhorst El-Flow, max 20 sccm Xe, precision 0.01 sccm) used as a performance reference. The cathode standalone testing is conducted in a vacuum chamber with internal dimensions of 60 × 30 × 30 cm. The chamber uses an inline combination of turbo-molecular and oil-based backing pump, achieving a background pressure of $< 1\times10^{-5}$ mbar without flow as measured by a cold cathode ionisation gauge (Leybold PTR90, 10^{-8} to 10^{3} mbar range). With propellant flow, the background pressure is within a range of $2.2–4.8\times10^{-4}$ mbar and $0.7–1.4\times10^{-4}$ mbar over the equal air and xenon mass flow rates tested respectively. The setup and equipment of the 'Icarus' chamber used at the University of Surrey's Plasma Propulsion Lab is shown in Fig. 4.

The input parameter range investigated during testing is shown in Table 1. The test procedure typically involves a sweep of anode plate bias at each combination of flow rate and microwave power values. A 2.45 GHz power sensor (Anritsu MA24105) is used to record the input microwave power at the cathode (P_{in}) during the test setup assembly, in order to quantify the power loss in the coaxial line (P_l). The 30, 60 and 90 W microwave generator forward powers (P_0) tested are found to correspond with input powers at the cathode of 24, 48 and 70 W respectively, via $P_{in} = P_0 - P_l$. As mentioned previously, the line is tuned to minimise reflected microwave power during cathode operation, typically to below 1 W. The true input power to the cathode is therefore slightly reduced by the power reflected, however this is not accounted for in the P_{in} calculation to retain conservative input power values that act as a common reference.

One source of uncertainty in the data collected is the variability in the AMPCAT plasma discharge, and this is assessed numerically using repeated measurements. The standard deviation of these readings is shown in the results presented later (see Figs. 5 and 6). Hardware uncertainties constitute another source of error in the inputs of bias voltage, microwave power and propellant flow to the cathode. In this case, the DC power supply manufacturers report an accuracy of ±16 mV in the voltage output for the negative cathode bias and a ±38 mA accuracy for the anode current reading. In the microwave circuit, the quoted generator output accuracy is ±1 mW, however a larger uncertainty of ±3.8% is reported for the inline meter used to measure the microwave power input to the AMPCAT. Finally, an accuracy of ±0.5% is provided for the mass flow controller (at room temperature).

3. Extracted current dependence on cathode bias

3.1. Dual current mode behaviour

The initial cathode prototype is tested in the standalone setup across the parameter range of Table 1. The extracted current with varying input microwave power is shown in Fig. 5, for a nominal $\dot{m} = 0.1$ mg/s of $0.48O_2$ + $0.52N_2$ air composition. The current values are averaged across repeated tests and plotted with error bars corresponding to the standard deviation in the measurements ($\pm\sigma$). This testing identifies a distinct transition between a lower- and higher-current mode which is prompted by increasing the total bias voltage, i.e. applying an increasingly negative cathode bias relative to the anode fixed at +20 V. The transition typically occurs in a V_b range of 70–90 V, resulting in an approximately ten-fold increase from $I_{extr} < 0.05$ A at $V_b = 40$ V to $I_{extr} > 0.5$ A at $V_b = 120$ V for the nominal 48 W input microwave power. It should be noted that the transition occurs in a discontinuous manner during a given voltage sweep. The threshold voltage lies within the 70–90 V range, as seen in Fig. 5 (the precise value is blurred due to the discrete V_b steps of 20 V). This is the reason for the larger error bars at 60 V and 80 V, since transition may occur at slightly different values between each acquisition. However, it can be seen that a high degree of repeatability exists in I_{extr} before and after the transition region, for instance if comparing the values at $V_b = 40$ V and 100 V. The current

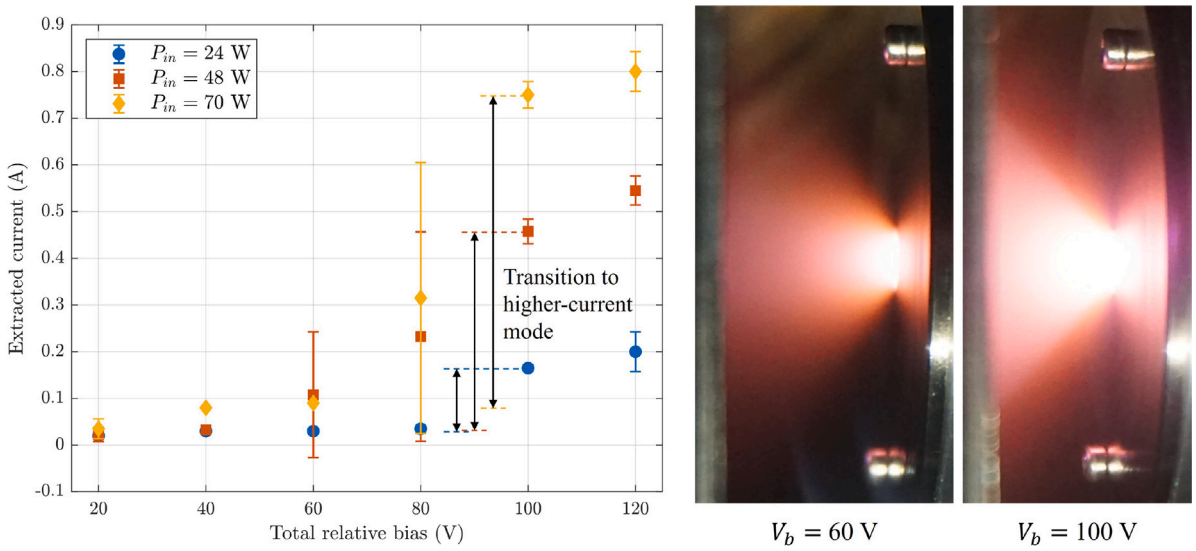

Fig. 5. Left: Extracted current with relative bias for initial prototype at $\dot{m} = 0.1$ mg/s of $0.48O_2$+$0.52N_2$ mixture. Error bars are plotted as $\pm\sigma$ around mean value from repeated tests and current transitions are qualitatively indicated between V_b = 40 V and 100 V values. **Right:** Corresponding air plasma discharge in orifice-anode region for lower- and higher-current mode at P_{in} = 48 W.

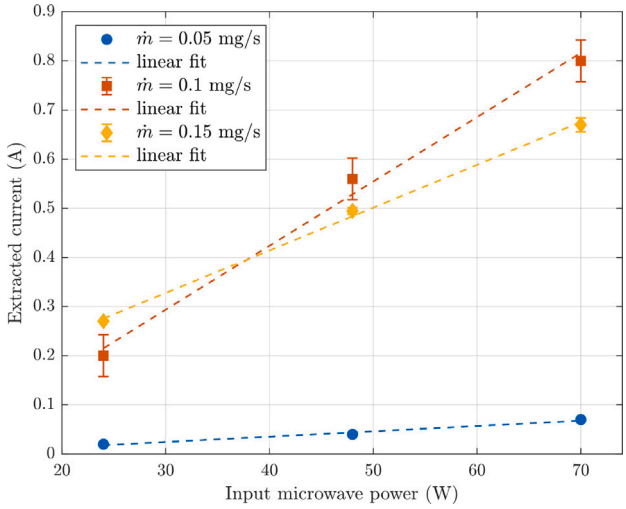

Fig. 6. Extracted current with microwave power for initial prototype at V_b = 120 V and $0.48O_2$+$0.52N_2$ mixture. Error bars are plotted as $\pm\sigma$ around mean value from repeated tests.

step is accompanied by a clear increase in the brightness of visible emission from the plasma discharge in the orifice-anode region, as also shown in Fig. 5. While the pink colour of the air plasma, associated primarily with the emission wavelengths of excited O and N neutrals, is maintained across the transition, there is a significantly brighter and more distinct plasma bridge visible between the internal cathode volume and the anode plate in the higher-current mode.

The current mode transition occurs at both $\dot{m}$ = 0.1 mg/s and $\dot{m}$ = 0.15 mg/s, however is not observed for the reduced 0.05 mg/s flow rate, as shown by the current data at V_b = 120 V plotted in Fig. 6. The extracted current in the higher-current mode appears generally linear with the input microwave power, as indicated by the linear fits included in Fig. 6. Such a relation between current and microwave power is advantageous for cathode operation, since the power input can be instantaneously adjusted with a digital command to the solid-state microwave generator, allowing maximum flexibility in the neutralising current available.

The identified dual current mode behaviour suggests a transition in the dominant electron production mechanism in the plasma between the lower- and higher-current modes. At low negative bias of the ion collection region, the emission of electrons occurs due to neutral ionisation in the vicinity of the microwave antenna. Electrons are heated by the oscillating E and B-fields within the skin-depth penetration of the microwaves into the plasma, as per Eq. (4). Since an estimated δ = 5.5 mm around the antenna extends to approximately one third of the 16.5 mm internal radius, electrons effectively diffuse throughout the cathode volume, leading to ionisation of neutral air particles via electron-impact. The resulting ions are collected by the negatively-biased walls, due to attraction by the negative potential gradient from the bulk plasma, resulting in an equal electron current which can be extracted from the discharge. This description is echoed by other microwave cathode literature, such as [29] and [28], using ECR-based electron-heating in the antenna vicinity for ionisation of xenon neutrals.

However, the significant increase in current suggests a source of fast electrons at higher bias values, resulting in increased ionisation. It is proposed that this occurs in the AMPCAT due to secondary electron emission (SEE) from the internal stainless steel surfaces. SEE results from impacts of charged or excited species with surfaces exposed to the plasma, leading to electron emission from the surface due to interactions with electrons in the upper band of the wall material. For instance, impacts of high-temperature electrons with the surface result in: (a) excitation of electrons in the material, (b) diffusion of these electrons to the surface, and (c) escape of sufficiently-excited electrons to free space by overcoming the surface potential, known as the work function ε_ϕ [41, p. 9:183–184]. Ion impacts with the surface yield either potential- (typically 10^1–10^2 eV order of impacting energy) or kinetic-based (typically > 10^3 eV) interactions with electrons in the material. In the potential case, the potential energy released during neutralisation of the ion by a primary electron provides sufficient energy for a secondary electron to escape the surface, such as in Auger emission [42, p. 302]. The criteria for this is based on the ionisation energy ε_{is} of the ion exceeding two times the work function:

$$\varepsilon_{is} > 2\varepsilon_\phi \tag{5}$$

For the cathode plasma, a predominantly atomic (rather than molecular) ion population is expected based on electron-neutral impacts. This is because the dissociation energies for O_2 and N_2 of 5.11 eV and 9.76 eV

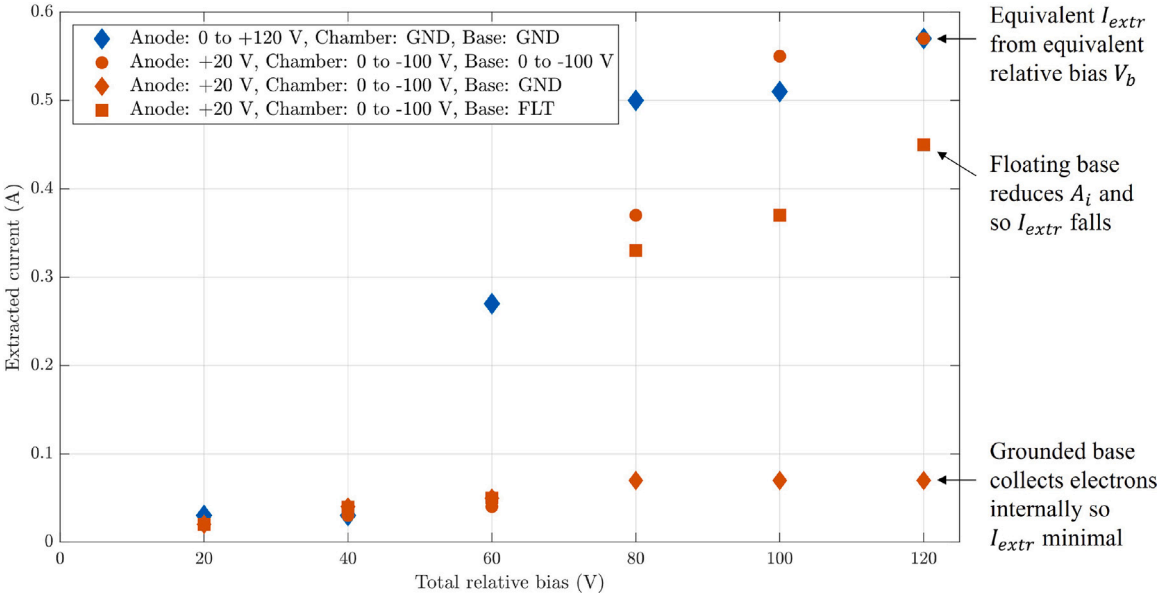

Fig. 7. Extracted current with relative bias for different biasing configurations, at $\dot{m} = 0.1$ mg/s of $0.48O_2$+$0.52N_2$ mixture and $P_{in} = 48$ W. 'Anode,' 'Chamber' and 'Base' refer to the biasing of the anode plate, internal chamber surfaces (& orifice plate) and cathode base respectively.

respectively [43,44], resulting in two atoms for every inlet molecule undergoing energetic electron-impact, are significantly lower than the respective first ionisation energy values of 12.21 eV and 15.63 eV [45, 46]. In the likely case of dissociation, the first ionisation energy is 13.62 eV for atomic oxygen and 14.53 eV for atomic nitrogen [47,48]. Ion-induced SEE can therefore occur for both O and N plasma species since the ionisation energies satisfy Eq. (5), for a stainless steel work function of $\varepsilon_\phi = 4.8$ eV [49]. Once a sufficient ion flux is reached due to the potential drop through the Child-Langmuir sheath in the ion collection region, a non-negligible degree of ion-induced SEE is supported from the stainless steel surface. For instance, data is recorded for a 100 eV oxygen ion impacting a molybdenum surface, which presents a similar $\varepsilon_\phi = 4.3$ eV value to the stainless steel used in the AMPCAT. This indicates an ion-induced SEE yield of $\gamma_i = 0.026$ [42, p. 303], with yield defined as the number of electrons released for every impacting particle.

Although this is a relatively small yield, the emitted electrons are accelerated away from the ion-collecting surface by the negative potential imposed at the wall, resulting in high-energy electrons released into the bulk plasma. These electrons might in turn impact other ion-collecting surfaces, since they are energetic enough to overcome the repulsive potential drop, and result in a significantly increased SEE yield. For example, a much larger electron-induced $\gamma_e \approx 0.65$ is observed for impacts of 100 eV electrons on grade 304 stainless steel [50]. Such a mechanism is identified by Oyarzabal et al. [51] for stainless steel surfaces exposed to a glow discharge at a pressure of $\sim 4 \times 10^{-3}$ mbar, which the authors use to explain an unexpectedly-large current at increased negative surface voltages. This is supported by measurements of a hot-tail in the electron energy distribution, for instance a $\sim 1\%$ fraction of $T_e = 180$ eV electrons in a thermal $T_e = 9$ eV population, whereby the small fraction sustains a significantly increased SEE from surfaces exposed to the plasma [52]. Indeed, the ion-induced SEE yield is generally constant with ion energy for the Auger potential-based emission that occurs at ion energies below $E_i \sim 10^3$ eV, i.e. γ_i for 10 eV ions is approximately equal to γ_i for those at 100 eV [53, p. 117]. The threshold bias needed for transition is therefore likely a combination of:

- a sufficient flux of ions to the walls, which increases with negative bias (see Eq. (2)). This generates a larger number of ion-induced emitted electrons.
- a sufficient acceleration of these electrons (from ion-induced SEE) into the bulk plasma, which also increases with negative bias. It is supposed that this acceleration becomes large enough for electrons to overcome the potential drop at the AMPCAT walls and so trigger large-scale electron-induced electron emission from the internal surfaces.

Consequently, at the point of transition, an electron avalanche in the cathode wall sheath results in emission of energetic electrons into the bulk plasma, with a high likelihood of exceeding the energy for electron-impact ionisation of air neutrals given an accelerating potential in the order of the −80 V surface bias. This stream of fast electrons therefore leads to a significantly higher degree of ionisation, explaining the dual current mode behaviour. Indeed, such a mechanism is proposed by Lisovskiy et al. [54] to support the transition from $\alpha-$ (low-current) to γ-regime (high-current) observed in a low-pressure oxygen RF conductively-coupled plasma (CCP) discharge. The authors record transition to the visually-brighter γ-regime occurring at an RF voltage of 92.1 V, for an oxygen pressure of $\sim 6 \times 10^{-2}$ mbar and a 13.56 MHz supply frequency. Given that the air pressure within the AMPCAT is measured as 4.4×10^{-2} mbar at the nominal $\dot{m} = 0.1$ mg/s flow rate (without plasma), there is a significant degree of similarity in the dual-current transition conditions between these two atmospheric gas-based discharges. A secondary electron emission mechanism, as detailed above, is therefore a possible explanation for the dual-current mode transition observed during AMPCAT operation.

3.2. Ion collection region biasing

Several biasing configurations for the internal cathode ion-collecting surfaces (see Fig. 1) are investigated to observe the resulting effect on the electron current extracted by the anode plate. The observed behaviour is shown in Fig. 7. First, it is confirmed that the same value of extracted current is recorded for a given relative bias between the anode and ion-collecting surfaces, for instance $I_{extr} = 0.57$ A at $V_b = 120$ V, for both: (a) cathode grounded and anode biased to +120 V, or (b) the nominal case of all cathode plasma-interfacing surfaces biased to −100 V and anode to +20 V. Subsequently, the cathode base is isolated and biased independently from the other ion-collecting surfaces. Tests are run with the base both floating and grounded, while the anode is biased at +20 V and the remaining ion-collecting

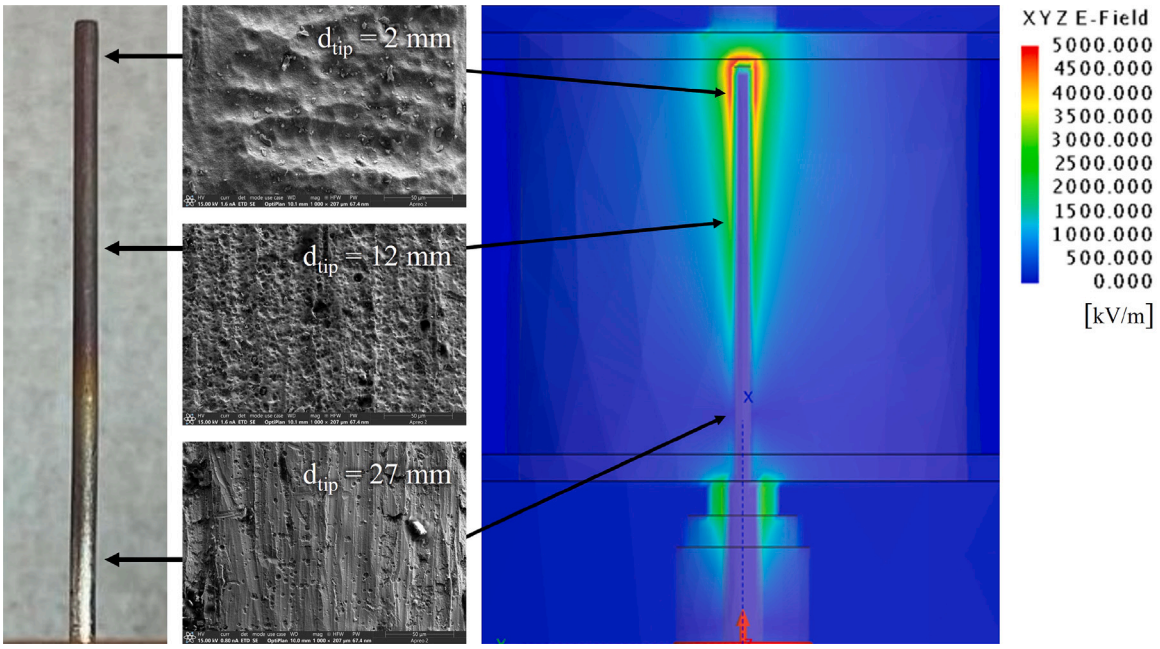

Fig. 8. Left: Post-test antenna after ~ 1 hour operation with $0.48O_2$+$0.52N_2$ mixture. **Centre-left:** SEM images of post-test antenna surface at x1000 magnification. **Right:** Simulation of antenna-induced E-field magnitude inside cathode at 60 W microwave power and without plasma, alongside $|E|$ scale.

region (plasma chamber and orifice plate) is biased negatively down to −100 V. Floating the base reduces the peak current by ~ 20%, since the total internal cathode area available for ion collection is decreased. Grounding the base significantly reduces the extracted current collected at the anode, down to a maximum of 0.07 A. However, a maximum ion current of 0.34 A is still collected on the other ion-collecting surfaces, suggesting that the grounded base acts as an electron-collector due to a relatively-positive bias compared to the other internal surfaces. The collection of a significant electron current on the base therefore vastly reduces the number of electrons reaching the anode, and so I_{extr}.

Table 2
Elemental composition (by percentage weight) along post-test antenna with distance to tip, measured using EDS analysis. $|E|$ from antenna simulation at 60 W input microwave power also shown.

d_{tip} (mm)	$\|E\|$ (V/m)	Mo (%)	O (%)	N (%)	C (%)	Fe (%)
2	5×10^6	74.3	17.8	2.5	3.1	1.7
12	3×10^6	75.3	16.2	2.6	3.8	1.1
22	1×10^6	66.3	14.0	4.4	9.5	3.1
27	3×10^5	89.0	4.6	0.0	4.6	1.4

4. Influence of antenna isolation

4.1. Antenna erosion

The exposed molybdenum antenna used in the initial prototype design is analysed after testing to study the effects of air plasma on the molybdenum surface, allowing a comparison of surface condition to simulations of the electric-field induced by the antenna. As described in Section 2.3, the antenna is electrically isolated from the upstream microwave line using a DC block. The antenna surface will therefore self-bias to prevent current being drawn from the plasma, and so the dominant E-field around the antenna is expected to originate from the simulated microwave radiation. As well as simulations, the antenna is imaged using scanning electron microscopy (SEM) to observe the surface topology, which includes an Energy dispersive X-ray spectroscopy (EDS) analysis to determine the elemental composition of the surface. The post-test antenna is shown in Fig. 8 alongside SEM images, at a magnification of 1000, for three visually-distinct regions of the antenna surface. The distance to the antenna tip is termed d_{tip}. Fig. 8 also includes a simulation of $|E|$ using commercial engineering software, modelling the prototype geometry without plasma and with an ideal (impedance-matched) 2.45 GHz coaxial input at 60 W microwave power. The variation of elemental weight fraction along the antenna length, obtained from the EDS analysis, is reported in Table 2, alongside the simulated E-field values. The principal elements observed are Mo, representing the antenna surface, O and N, accounting for the plasma species, C, likely introduced during antenna machining for assembly, and Fe, which forms the primary component of the grade 304 stainless steel internal surfaces.

Looking at the post-test images, the dull region around the tip of the antenna, where the maximum $|E| = 5 \times 10^6$ V/m occurs, suggests sputtering of the surface due to impacts of high-energy air species, which is supported by the heavily cratered surface visible in the SEM. Further along the antenna, a decreasing $|E|$ corresponds to a reduced level of sputtering, which is shown by the smaller diameter and depth of craters in the d_{tip} = 12 mm SEM image. There is a high oxygen content of 16–18% and significantly lower nitrogen content throughout the sputtered region of the antenna surface, likely due to the higher reactivity of oxygen leading to retention on the surface. This is supported by literature on sputter yields for O^+ and N^+ impacting a Mo surface, which predicts both: (a) a lower threshold ion energy for oxygen of 40 eV compared to 70 eV for nitrogen, and (b) an order of magnitude higher sputter yield (surface atoms released per impacting ion) for O^+, e.g. ~ 4×10^{-2} at a 100 eV ion energy compared to ~ 5×10^{-3} for N^+ [55]. Around d_{tip} = 22 mm, the visual colouring and increased Carbon content suggests that sputtering, less prevalent due to an $|E|$ around 5 times lower than at the tip, is replaced by a high surface temperature as the driver of surface characteristics. Towards the antenna base, the visual image shows a reflective surface with little difference to before the test. This links to a simulated $|E|$ value that is one order of magnitude below that at the tip and significantly less surface erosion, likely due to reduced local particle energies below the sputtering threshold. The visual image is supported by the EDS and

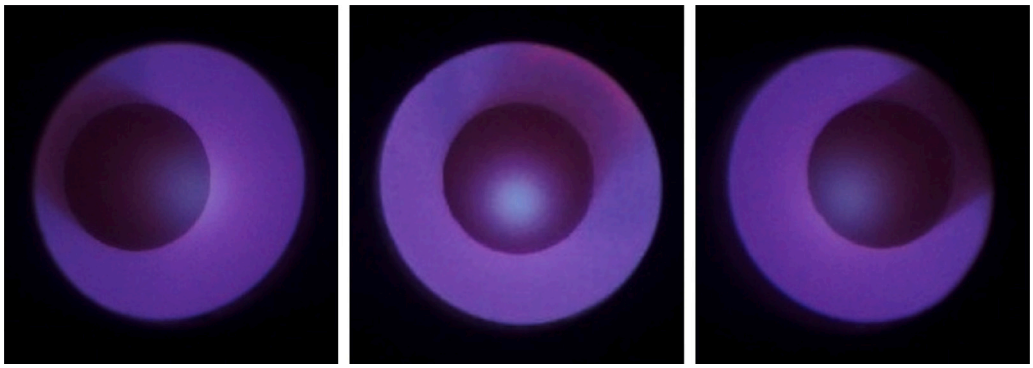

Fig. 9. Images from varying angles of internal cathode discharge through extraction orifice, at $I_{extr} = 0.43$ A with 0.1 mg/s of Xe at $P_{in} = 48$ W and $V_b = 40$ V.

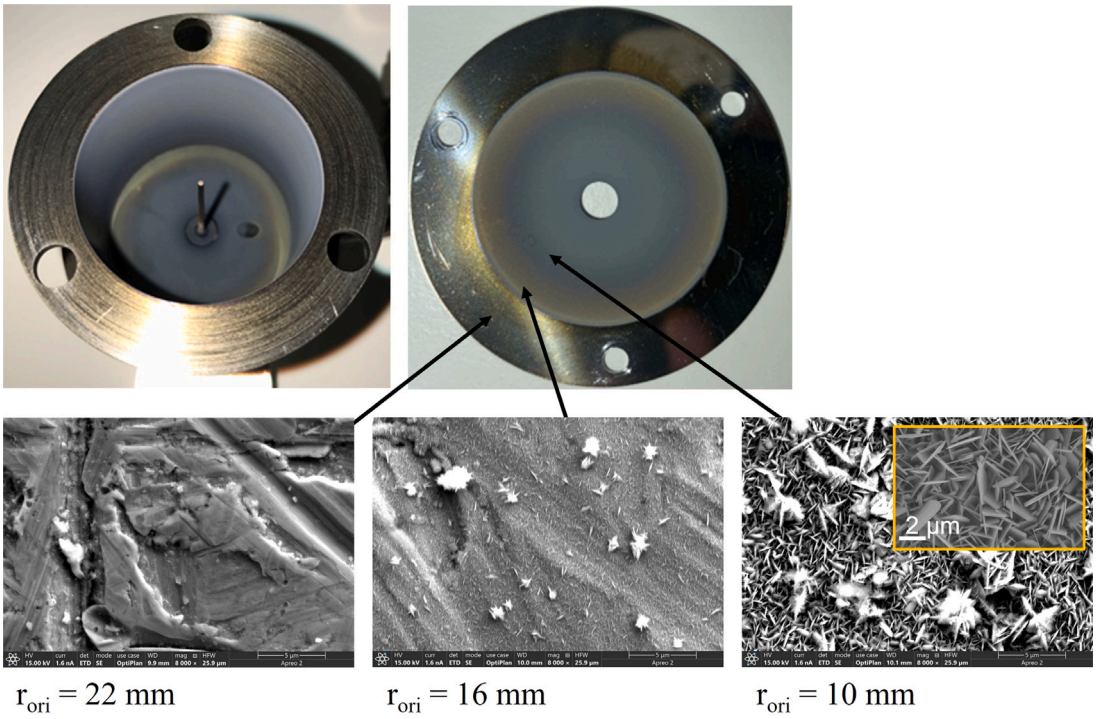

Fig. 10. Upper: Post-test cathode internal volume and orifice plate after ~ 1 hour operation with $0.48O_2$+$0.52N_2$ mixture. **Lower:** SEM images of post-test orifice plate (internal surface) at x8000 magnification, for three radial locations. Inset on $r_{ori} = 10$ mm image shows MoO_3 platelet deposition at same scale, from [56].

SEM analyses, which indicate a high-purity Mo surface and features corresponding to the grooves introduced during antenna manufacture.

The high E-field at the tip of the antenna, suggested by the $|E|$ simulation and antenna erosion analysis, is also supported by images of the cathode discharge taken through the extraction orifice. These are presented in Fig. 9 at varying angles in order to show an observed region of increased brightness marginally downstream of the antenna tip. The images are obtained using an anode plate with a 15 mm diameter central opening, through which the internal cathode discharge is viewed, having verified that an equivalent extracted current is measured compared to the usual full plate. The visible region of increased plasma emission intensity also indicates a maximum degree of ionisation in the antenna tip vicinity.

4.2. Internal surface coating

During testing with the exposed Mo antenna and the $0.48O_2$ + $0.52N_2$ mixture, a non-conductive blue-grey coating is found to develop on the internal cathode surfaces, leading to decreasing extracted current with test duration. The internal coating resulting from approximately one hour of cathode operation across the test input range is shown at the top of Fig. 10. Similarly to the antenna, an SEM analysis is performed on the internal surface of the orifice plate to analyse this coating, which is present on the plasma-exposed area in comparison to an uncoated stainless steel surface where the plate is tightly bolted to the ion-collector.

The orifice plate is imaged at varying radial locations, based on the distance from the orifice centre r_{ori}, for which the surface at 8000 times

Table 3
Elemental composition (by percentage weight) with radius of post-test orifice plate, measured using EDS analysis.

r_{ori} (mm)	Mo (%)	O (%)	N (%)	Fe (%)	Cr (%)	Ni (%)
3	68.7	27.4	2.8	0.4	0.0	0.2
10	68.5	25.6	2.8	2.0	0.6	0.2
16	34.3	17.2	2.1	31.4	9.8	3.0
22	1.1	2.3	0.5	66.3	18.7	7.2

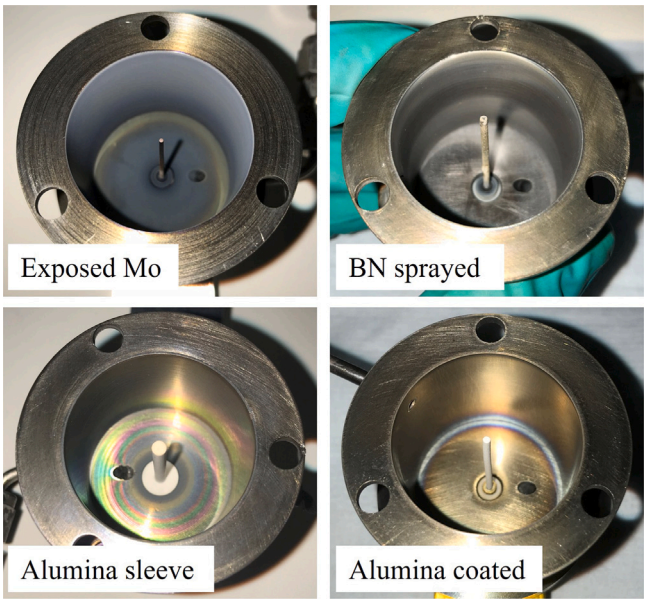

Fig. 11. Images of internal cathode volume after ~ 1 hour operation with $0.48O_2$+$0.52N_2$ mixture for varying levels of antenna isolation. **Clockwise from upper-left:** Exposed Mo antenna as per initial design, boron-nitride spray coating, alumina plasma coating and alumina machined antenna sleeve.

magnification is shown at the bottom of Fig. 10. An EDS analysis reveals the elemental composition with r_{ori}, as detailed in Table 3 for the six most prominent species. The uncoated region at r_{ori} = 22 mm shows grooves from the machining process and a composition that matches closely with the expected values for grade 304 stainless steel, typically 67–71% Fe, 18–20% Cr and 8–11% Ni [39].

The well-coated region at r_{ori} = 10 mm is shown in the right-hand SEM image of Fig. 10, revealing platelets covering the surface and an elemental composition of 69% Mo and 26% O. This suggests the coating is a molybdenum-oxide, which is supported by the similarity of the surface topography and elemental composition to SEM analysis of MoO_x in literature, such as the inset at r_{ori} = 10 in Fig. 10 which shows MoO_3 platelets imaged in [56]. Given the antenna erosion detailed previously, the coating likely originates due to Mo species sputtered from the antenna and oxidised. The r_{ori} = 16 mm SEM image, on the boundary of the coated region, shows the initial development of the MoO_x coating on the stainless steel cathode surfaces.

4.3. Antenna isolation methods

The cathode design is adjusted to mitigate the non-conductive coating identified in the previous Section. It is found that electrically isolating the molybdenum antenna from the plasma avoids formation of the MoO_x coating on internal surfaces, allowing continuous cathode operation without a decreasing current with time. The concept is initially verified by applying a boron-nitride spray to the antenna, the effect of which is compared to the initially exposed Mo antenna in Fig. 11, imaged after approximately one hour of testing with air. While the coating is significantly reduced, a degree appears towards the end of testing due to fracturing of the BN spray coating from heating of the underlying antenna. Two solutions for antenna isolation are therefore identified for a high antenna temperature: (a) a machined alumina sleeve, with a wall thickness range of 0.5–0.7 mm, and (b) plasma coating of the antenna with alumina to thicknesses of 0.1–0.3 mm, using an atmospheric plasma spray process. These configurations are similarly shown after equivalent testing in Fig. 11, indicating the successful alleviation of the coating phenomenon through preservation of high-conductivity, clean stainless steel walls and an isolating, clean ceramic collar at the base of the antenna.

Table 4
Pre- and post-test elemental composition (by percentage weight) at mid-length between alumina-coated antenna and machined alumina sleeve, measured using EDS analysis.

Antenna type	O (%)	Al (%)	N (%)	C (%)
Coat, pre-test	48.1	48.0	0.6	2.8
Coat, post-test	46.0	48.1	2.7	1.8
Sleeve, pre-test	59.8	24.5	1.9	13.2
Sleeve, post-test	55.9	13.7	8.8	8.2

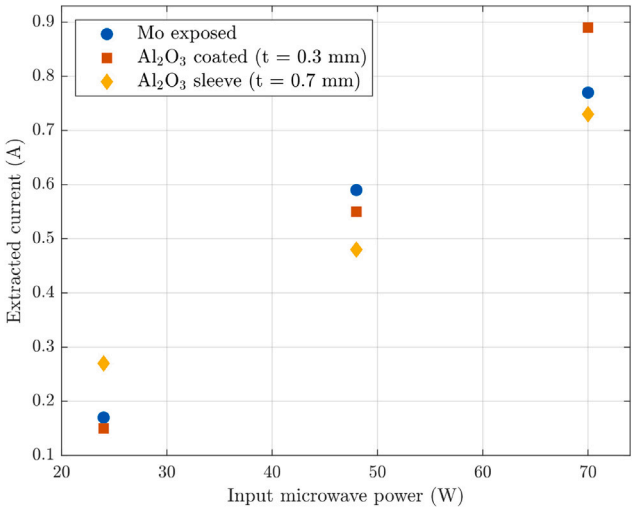

Fig. 12. Extracted current with microwave power for varying antenna isolation, at V_b = 120 V and $\dot{m}$ = 0.1 mg/s of $0.48O_2$+$0.52N_2$ mixture.

The elemental composition of both the plasma-coated and machined-sleeve alumina isolation approaches is analysed using EDS before and after around one hour of cathode operation with $0.48O_2$ + $0.52N_2$. The fractions of the four major elements present are reported in Table 4, with a maximum error of 0.3% and 1.1% evaluated by the EDS software for the 'coated' and 'sleeve' spectra respectively. This data shows that the alumina-coated antenna displays only minor surface composition changes because of exposure to air plasma during cathode operation, with a marginal increase up to 3% in the nitrogen content due to retention of plasma species. The machined sleeve undergoes a slightly increased change in composition due to testing, however again this appears to be primarily driven by N retained on the surface, from a 2% to 9% fraction. In both cases, a significantly increased oxygen fraction resulting from plasma exposure is avoided, thus mitigating the issues observed with the exposed molybdenum antenna. This supports a stable electrically-isolating layer around the antenna, preventing the detrimental sputtering-based coating mechanism.

The two antenna isolation configurations are pursued since $|E|$ simulations show no significant differences in the antenna-induced electric-field relative to the exposed Mo antenna case. This is verified via standalone testing, which demonstrates that both the isolated antenna configurations support an equivalent level of current extraction compared to the exposed antenna. This is the case across the range of input microwave power and air mass flow rate, which is shown in Fig. 12 for a total relative bias of 120 V at the nominal flow rate. The current behaviour supports the assumption that electron heating via microwaves occurs primarily in a layer around the antenna corresponding to the plasma skin depth, expected in the $\delta \approx 5.5$ mm ballpark (see Section 2.1), therefore a relatively small dielectric thickness of $t \leq 0.7$ mm does not significantly impact microwave power-coupling to the plasma in the antenna near-field.

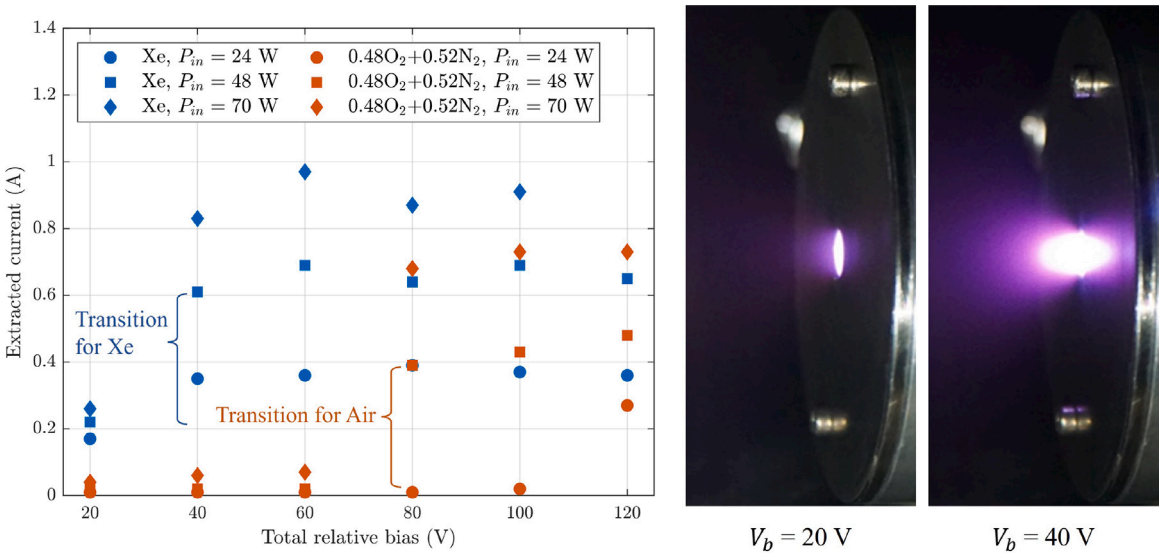

Fig. 13. Left: Extracted current with relative bias for varying input microwave power, comparing $\dot{m}$ = 0.1 mg/s of Xe and $0.48O_2$+$0.52N_2$ mixture with t = 0.7 mm alumina machined antenna sleeve. **Right:** Corresponding Xe plasma discharge in orifice-anode region for lower- and higher-current mode at P_{in} = 48 W.

5. Influence of propellant

The current extraction in standalone testing is analysed using xenon as propellant, in order to compare the cathode performance on air with a noble gas reference conventionally reported in literature. This is done for the isolated antenna configuration through matching mass flow rates between Xe and the $0.48O_2$ + $0.52N_2$ mixture, for instance resulting in a volumetric inlet flow rate of 1.0 sccm and 4.7 sccm respectively for an $\dot{m}$ = 0.1 mg/s comparison. Mass flow rate matching is used since this is a key parameter in calculating the performance metrics of the overall thruster system. The extracted current collected on the anode with relative bias is shown for both propellants in Fig. 13, at varying microwave power levels and using the machined alumina antenna sleeve configuration. As indicated in the figure, transition from lower- to higher-current mode occurs for both air and xenon, with an approximately three-fold jump in current from I_{extr} = 0.22 A at V_b = 20 V to I_{extr} = 0.61 A at V_b = 40 V for the nominal P_{in} = 48 W with Xe. The corresponding increased visible emission of the characteristically blue-purple cathode plasma is also shown Fig. 13. Transition is found to occur at a lower bias for xenon, by V_b = 40 V for the full range of P_{in} compared to 80 V for air at higher powers, as well as a peak current around 30–40% higher than at the same microwave power for air. It is noted that transition in this case is delayed to a higher bias for operation with air at the lowest power of P_{in} = 24 W. This suggests that the component of ionisation originating from microwave coupling into the plasma at this power level is insufficient to maintain a self-sustained discharge in the higher-current mode, likely due to molecular energy-losses, thereby requiring a higher V_b value to trigger transition.

The presence of the dual-current behaviour with xenon, as for air, is expected based on the SEE-driven mechanism proposed in Section 3.1, since the 12.13 eV first ionisation energy of xenon also satisfies the secondary emission criteria of Eq. (5) (for a stainless steel ε_ϕ = 4.8). The ion-induced secondary electron emission yield is similar for both singly-charged oxygen and xenon ions, for instance γ_i = 0.026 and γ_i = 0.019 respectively in the case of 100 eV ions impacting a molybdenum surface [53, p. 117]. Since these values are representative for the stainless steel cathode surfaces, the differences in extracted current behaviour likely originate from the ionisation characteristics of xenon and air species. In the case of electron-neutral collisions, the dominant ionisation mechanism expected in the cathode, the electron-neutral collision frequency depends on the electron-neutral ionisation collision cross-section. This is a function of T_e and the neutral particle species. Since air species in the cathode plasma are expected to be dissociated (see Section 3.1), the relevant first ionisation energy values are 13.62 eV for atomic oxygen and 14.53 eV for nitrogen [47,48]. If assuming a T_e = 15 eV electron (e.g. in the high-energy tail of the distribution function for electrons in the antenna vicinity) sufficient for ionisation of O, N and Xe, the electron-impact cross-sections are 1.28×10^{-21} m^2, 1.10×10^{-21} m^2 and 1.15×10^{-20} m^2 respectively [57–59]. Given that the collision-frequency is directly proportional to the cross-section, the expected rate of potentially-ionising collisions in this case is 7.1 times higher for Xe than O and 8.2 times higher than for N. In the case of electron-neutral collisions for air, electron energy is lost for dissociation of O_2 and N_2 into their atomic species, as well as in additional molecular excitations, such as vibrational and rotational modes. For instance, Lieberman and Lichtenberg [42, p. 82] note that the energy lost for an ion-electron pair created (from an ionisation collision) is generally 2–10 times larger in a molecular gas than an atomic equivalent at electron energies below 7 eV. As a result, a significantly higher degree of ionisation occurs for xenon, yielding an increased ion density in the bulk plasma. This supports both the key differences identified in Fig. 13: (a) transition to the higher-current mode at a lower bias with xenon than with air, since the ion flux is higher at a given wall voltage, prompting sufficient ion-induced SEE, and (b) larger extracted current values with xenon, since the increased plasma density allows an increased electron current to be extracted from the cathode.

6. Prototype development for continuous operation

The AMPCAT neutraliser design is evolved through iterative standalone testing, as detailed in the preceding sections. This results in a refined prototype design, which aims at continuous operation on air in the hours timescale and with a consistent extracted current level. A description of the isolation configurations for the $\lambda/4$ molybdenum antenna is given in Section 4.3, namely the use of an antenna plasma-coated with an alumina layer or an alumina machined sleeve into which the antenna is inserted. Several coated antennas with coating thicknesses in the 0.1–0.3 mm range are tested, without a significant observed effect of isolation thickness on extracted current performance. The finalised machined sleeve design features a t = 0.5 mm wall thickness and a conical base to relieve stress concentrations in the thin ceramic part during assembly. A key limiting factor on cathode operation is excessive heating of the PTFE dielectric used in the off-the-shelf microwave connector. This was found to soften and deform

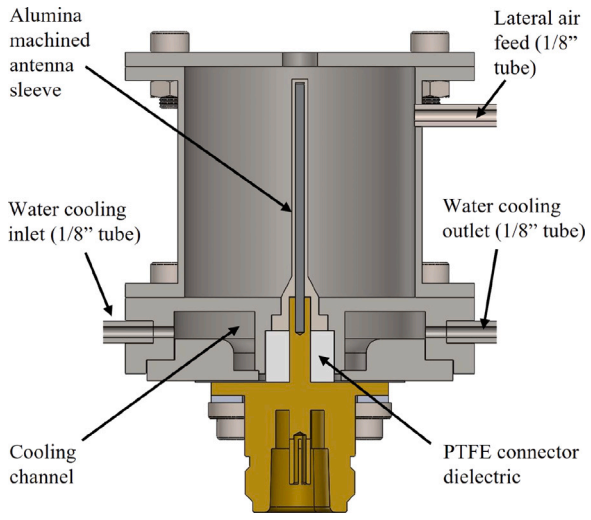

Fig. 14. Cross-section design of refined AMPCAT prototype, with machined alumina antenna sleeve shown.

Table 5
Operating parameters for standalone duration tests, with finalised prototype using $t = 0.1$ mm Alumina plasma-coated antenna.

Source MW power (W)	60	90
Input MW power (W)	48	70
Internal bias (V)	−60	
Anode bias (V)	+20	
Air mass flow rate (mg/s)	0.1	
Air composition	$0.48O_2$ +$0.52N_2$	
Background pressure in chamber (mbar)	3.4×10^{-4}	
Test duration (mins)	120	
Extracted current (A)	0.52–0.56	0.79–0.80
Reflected MW power (W)	3	4
Stabilised temperature at MW connector	53	68
Average C_e (mA/W)	7.0	6.9
Average $1/C_e$ (W/A)	142.1	144.8
Average U_i	1.7	2.4

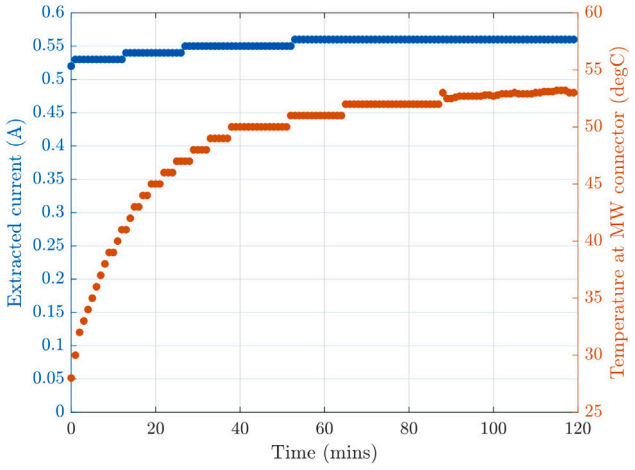

(a) $P_{in} = 48$ W.

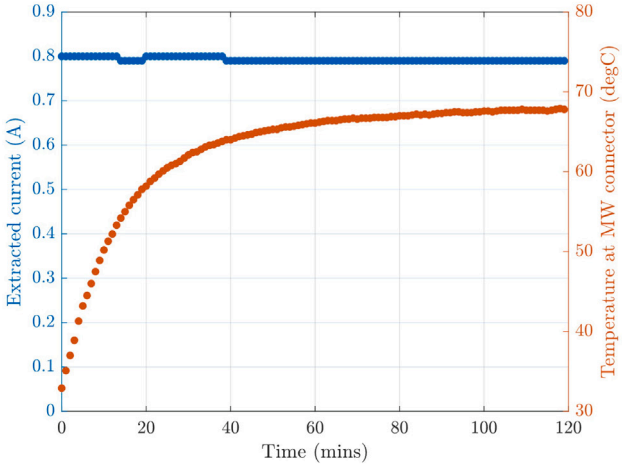

(b) $P_{in} = 70$ W.

Fig. 15. Extracted current and microwave connector temperature with time for two-hour duration tests at $\dot{m} = 0.1$ mg/s of $0.48O_2$+$0.52N_2$ mixture and constant $V_b = 80$ V.

at temperatures exceeding ∼ 150 °C, as measured by a thermo-couple on the connector housing (see Fig. 2), leading to reduced microwave transmission. As a result, water-cooling is implemented via an internal channel in the stainless steel cathode part housing the connector, with water supplied to transfer heat from the PTFE dielectric. A minimised wall thickness of 1.5 mm is used between the PTFE and cooling channel to increase conductive heat transfer, and this is visible in the refined prototype design shown in Fig. 14. The use of a high-temperature microwave connector is foreseen in future prototype iterations to avoid the use of active cooling.

6.1. Duration testing

The continuous operation of the refined prototype is evaluated in two tests, each conducted for a duration of two hours. In this case, a $t = 0.1$ mm alumina coated antenna is used and water-cooling is provided by an external chiller running at a pressure of 3 bar. The tests are run at 48 W and 70 W input microwave powers to demonstrate current levels of 0.5 A and 0.8 A respectively, for a constant internal cathode bias of −60 V and +20 V bias on the anode. The operating parameters are detailed in Table 5. The water-cooling results in an allowable stable temperature at the microwave connector interface to the cathode, with a plateau around 53 °C and 68 °C for operation at 0.5 A and 0.8 A respectively, comfortably below a temperature of ∼ 150 °C at the same location for which dielectric deformation is found to occur. The current and temperature profiles for both tests are shown in Figs. 15(a) and 15(b). Both tests are deliberately terminated, rather than due to any changes in cathode operation, and post-test inspections show neither visible damage to the PTFE dielectric nor any noticeable coating of the plasma-interfacing surfaces of the cathode and anode.

6.2. Standalone performance comparison

The current extraction performance of the refined AMPCAT prototype is characterised across the full range of microwave power and air mass flow rate. This standalone extracted current data is presented in Fig. 16(a), alongside the power and propellant usage figures of merit; C_e in Fig. 16(b) and U_i in Fig. 16(c). It should be noted that C_e and C_e^{-1} are calculated including microwave power and the DC power linked to the negative biasing of the cathode internal surfaces, however without including the DC power needed to bias the anode (as for Table 5), since: (a) the anode reproduces the potential gradient that will be provided by the thruster discharge in a coupled scenario, and (b) the anode power depends on the specific geometry of the anode and its distance to the cathode orifice. The standalone test data demonstrates the ability to extract a current approaching 1 A with air propellant across the 0.05–0.15 mg/s mass flow rate range, at a 70 W microwave input power.

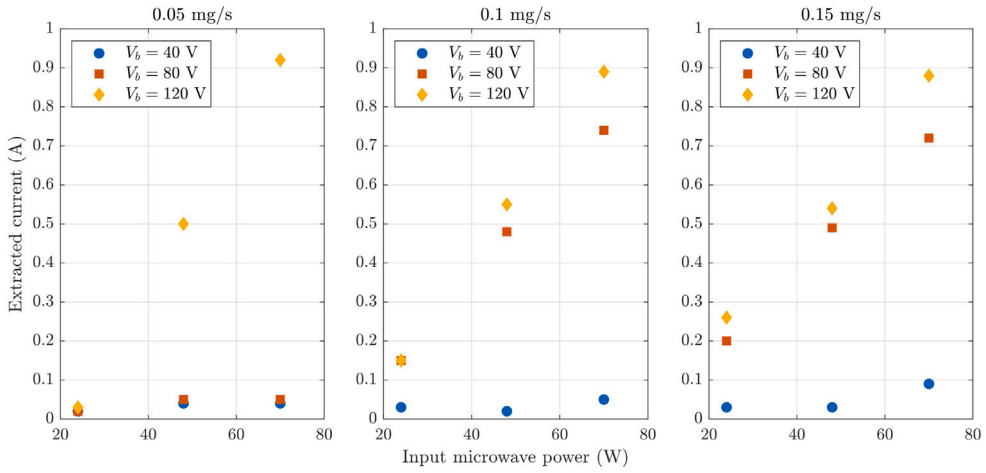

(a) Extracted current (I_{extr}).

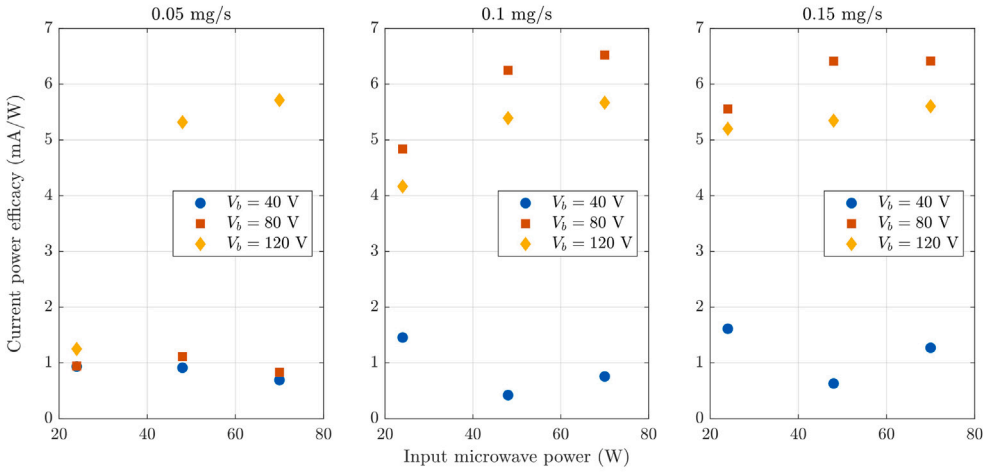

(b) Current power efficacy (C_e).

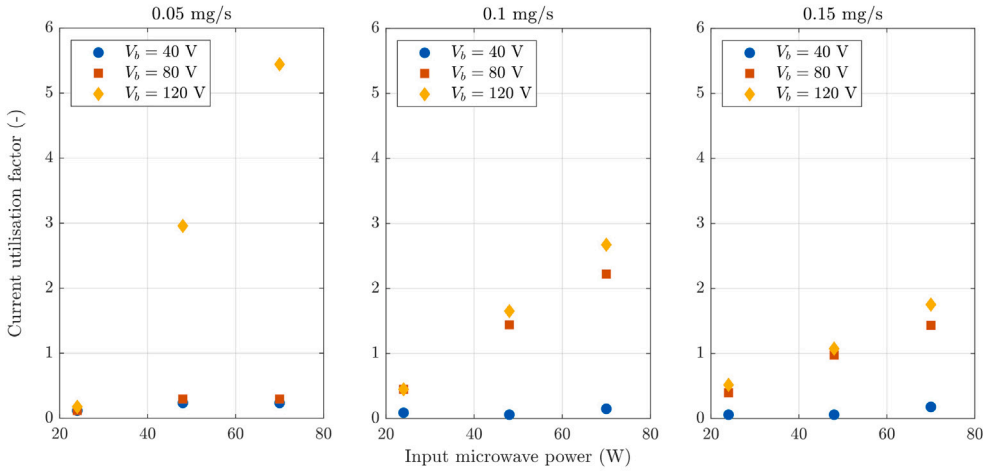

(c) Current utilisation factor (U_i).

Fig. 16. Standalone AMPCAT prototype performance with varying microwave power and mass flow rate of $0.48O_2$+$0.52N_2$ mixture, at different total relative bias values, using $t = 0.3$ mm alumina coated antenna. AMPCAT C_e & C_e^{-1} values do not include power contribution from extracting anode.

As noted previously, there is a broadly linear relationship between I_{extr} and input microwave power at increased bias values where the discharge is in the higher-current mode. The best-case power efficacy C_e is found to occur at the threshold voltage for transition and drops with increasing V_b after this point. The fact that C_e is generally more constant with microwave power, for instance C_e = 5–6.5 mA/W at $\dot{m}$ = 0.15 mg/s, suggests that higher extracted current values are attainable with increased microwave power, since a drop-off in efficiency of the microwave power coupling into the plasma is not seen up to the 70 W tested. The propellant utilisation decreases at higher flow rates and is noticeably maximised for operation in the higher-current mode with $\dot{m}$ = 0.05 mg/s.

Table 6
Comparison of AMPCAT prototype performance to cathodes from literature, for standalone testing and cathode total power below 300 W. AMPCAT inputs for maximising I_{extr}, C_e and U_i individually shown in **bold**. Extracting anode power contribution is not included in C_e & C_e^{-1} values for AMPCAT and [20], however is included for [21,28,33,60].

Cathode	Gas	$\dot{m}$ (mg/s)	P_{tot} (W)	I_{extr} (A)	C_e (mA/W)	C_e^{-1} (W/A)	U_i
Typical W filament [32]	Xe	0.3	60	0.30	5.0	200	1.0
Typical HCN LaB6 [32]	Xe	0.2	130	4.0	30.0	33	28.0
RF ICP [21]	Xe	0.3	114	1.7	14.9	67	7.9
MW ECR [28]	Xe	0.3	258	2.6	10.2	98	12.2
MW ECR (μ10) [60]	Xe	0.07	13.8	0.18	13.1	76	3.6
MW ECR (μ20) [33]	Xe	0.1	45	0.50	11.1	90	7.0
DC (E × B) [20]	Air	0.08	89	0.24	2.7	370	1.1
AMPCAT w/ Xe							
P_{in} = 70 W, V_b = 60 V	Xe	0.1	126	**0.97**	8.9	112	13.3
P_{in} = 24 W, V_b = 30 V	Xe	0.1	34.5	0.35	**12.7**	79	4.8
P_{in} = 48 W, V_b = 80 V	Xe	0.05	100	0.68	7.7	131	**18.6**
AMPCAT w/ Air							
P_{in} = 70 W, V_b = 120 V	Air	0.1	176	**0.90**	5.6	178	2.7
P_{in} = 70 W, V_b = 80 V	Air	0.1	128	0.74	**6.5**	155	2.2
P_{in} = 70 W, V_b = 120 V	Air	0.05	177	0.90	5.6	178	**5.3**

A comparison of the AMPCAT prototype to other low-power alternative neutralisers in the literature is shown in Table 6. As previously, the DC extracting anode power is not included in the AMPCAT C_e and C_e^{-1} values, however it should be noted that this is not possible to do for the other microwave and RF cathodes referenced in Table 6 [21,28,33,60] due to their standalone test configurations of a grounded cathode and bias applied solely to the anode. The performance with xenon compares well in maximum efficiency values (C_e and U_i) with the reported performance of the JAXA microwave ECR neutraliser [33,60]. While data on cathode operation with air is scarce, a significant increase in current and efficiency values is observed in comparison to a DC cathode using air presented in [20]. Overall, the cathode performance demonstrated in this initial study bodes well for satisfying the current requirements of an air-breathing propulsion system.

7. Conclusion

A cathode operating on air is developed, termed the AMPCAT, in the framework of the AETHER project's design of an air-breathing electric propulsion system for VLEO. This study presents the evolution of the microwave plasma cathode design based on iterative standalone testing. A particular area of focus is the antenna erosion and internal surface coating resulting from direct insertion of the molybdenum antenna into the air plasma, which is mitigated through the use of an electrically-isolating alumina layer around the antenna. A dual-current mode is identified in the cathode extracted current with increasing relative bias between the internal surfaces and extracting anode, resulting in an order of magnitude increase in current at $V_b > 80$ V for a $0.48O_2 + 0.52N_2$ air mixture. A secondary electron emission-based mechanism is proposed to explain the current transition, leading to an electron avalanche at the ion-collecting internal walls and a high-energy electron population which supports significantly increased ionisation in the bulk plasma. In general, extracted current values greater than 0.5 A and 0.9 A are demonstrated across the 0.05–0.15 mg/s range of air mass flow rates for 48 W and 70 W input microwave powers respectively. A performance comparison with xenon as a reference yields an equivalent dual-current behaviour, with a reduced transition bias of around 40 V and a 30–40% increase in peak extracted current based on more effective ionisation. The cathode prototype is developed to a refined design, which demonstrates stable current extraction with air at 0.8 A over several hours of operation. Future work foresees a validation of the cathode electron emission in supporting a thruster discharge, for which thrust-balance tests using a low-power Hall-type thruster are planned with comparison to a conventional hollow cathode. A study of the AMPCAT dual-current mode behaviour is also anticipated via plasma diagnostics of the internal and external cathode discharge.

Declaration of competing interest

The authors declare that they have no known competing financial interests or personal relationships that could have appeared to influence the work reported in this paper.

Acknowledgements

This work has been partly performed within the AETHER project, funded by the EU's Horizon 2020 research and innovation programme under grant agreement No. 870436. This reflects only the author's view and the European Commission is not responsible for any use that may be made of the information it contains. The authors would like to thank Vittorio Giannetti for his support of the project and acknowledge all the members of the AETHER consortium for the exciting work undertaken together. Thanks go to RHP-Technology GmbH for the antenna coating and, in particular, to the Propulsion Lab Technical Support and Mechanical Engineering Workshop teams at Surrey for lab maintenance and manufacture of cathode prototype components. The authors particularly acknowledge Brian Eades for his patience and high-quality machining. Finally, Mansur Tisaev thanks the Doctoral College of the University of Surrey for his Ph.D. scholarship funding.

References

[1] N. Crisp, et al., The benefits of very low earth orbit for earth observation missions, Prog. Aerosp. Sci. 117 (2020) 100619, http://dx.doi.org/10.1016/j.paerosci.2020.100619.
[2] Alenia Spazio, GOCE system critical design review (CDR), 2005, URL http://esamultimedia.esa.int/docs/GOCE_System_Critical_Design_Review.pdf.
[3] S. Imamura, et al., Analysis of upper atmospheric effects on material per onboard atomic oxygen monitor system of SLATS, Front. Space Technol. 3 (2022) http://dx.doi.org/10.3389/frspt.2022.891753.
[4] M. Tisaev, E. Ferrato, V. Giannetti, C. Paissoni, N. Baresi, A. Lucca Fabris, T. Andreussi, Air-breathing electric propulsion: Flight envelope identification and development of control for long-term orbital stability, Acta Astronaut. 191 (2022) 374–393, http://dx.doi.org/10.1016/j.actaastro.2021.11.011.
[5] V. Hruby, K. Hohman, J. Szabo, Air breathing hall effect thruster design studies and experiments, in: 37th International Electric Propulsion Conference, Cambridge, USA, 2022, URL https://www.jotform.com/uploads/electricrocket/220994246997171/5312870890131990576/IEPC%202022-446%20Hruby.pdf.
[6] K. Nishiyama, Air breathing ion engine, in: Proc. of 24th International Symposium on Space Technology and Science, Miyazaki, Japan, 2004, URL https://ci.nii.ac.jp/naid/10014931545/en/.
[7] K. Fujita, Air intake performance of air breathing ion engines, J. Japan Soc. Aeronaut. Space Sci. 52 (610) (2004) 514–521, http://dx.doi.org/10.2322/jjsass.52.514.
[8] D. Di Cara, J. Gonzalez del Amo, et al., RAM electric propulsion for low earth orbit operation: An ESA study, in: 30th International Electric Propulsion Conference, Florence, Italy, 2007, URL http://electricrocket.org/IEPC/IEPC-2007-162.pdf.
[9] E. Ferrato, et al., Development roadmap of sitael's RAM-EP system, in: 36th International Electric Propulsion Conference, Vienna, Austria, 2019, URL http://electricrocket.org/2019/886.pdf.
[10] T. Andreussi, E. Ferrato, V. Giannetti, A review of air-breathing electric propulsion: from mission studies to technology verification, J. Electr. Propuls. 1 (31) (2022) http://dx.doi.org/10.1007/s44205-022-00024-9.
[11] T. Andreussi, et al., The AETHER project: development of air-breathing electric propulsion for VLEO missions, CEAS Space J. (2022) http://dx.doi.org/10.1007/s12567-022-00442-3.
[12] P. Crandall, R. Wirz, Air-breathing electric propulsion: mission characterization and design analysis, J. Electr. Propuls. 1 (1) (2022) http://dx.doi.org/10.1007/s44205-022-00009-8.
[13] S. Vaidya, C. Traub, F. Romano, G. Herdrich, et al., Development and analysis of novel mission scenarios based on atmosphere-breathing electric propulsion (ABEP), CEAS Space J. 14 (4) (2022) 689–706, http://dx.doi.org/10.1007/s12567-022-00436-1.

[14] T. Andreussi, et al., Characterization of an atmospheric propellant-fed hall thruster as a VLEO simulator, in: 37th International Electric Propulsion Conference, Cambridge, USA, 2022, URL https://www.jotform.com/uploads/electricrocket/220994246997171/530526449252955141O/IEPC_2022_AETHER_final.pdf.
[15] D. Goebel, I. Katz, Fundamentals of Electric Propulsion: Ion and Hall Thrusters, First, Wiley, 2008.
[16] H. Gallagher, Poisoning of LaB6 cathodes, J. Appl. Phys. 40 (1) (1969) 44–51, http://dx.doi.org/10.1063/1.1657092.
[17] J. Cronin, Practical aspects of modern dispenser cathodes, Microw. J. (1979) URL https://www.cathode.com/pdf/tb-134.pdf.
[18] C. Drobny, J.-P. Wulfkühler, K. Wätzig, M. Tajmar, Endurance test of a hollow cathode using the emitter material C12a7 electride, in: Space Propulsion 2020+1, Online, 2021, URL https://www.researchgate.net/publication/351051549.
[19] D. Zschätzsch, M. Reitemeyer, P. Klar, A. Post, J. Fernandez, Design and operation of a hollow cathode with a C12a7:2e- insert in comparison with a LaB6 insert, in: 37th International Electric Propulsion Conference, Cambridge, USA, 2022, URL https://www.jotform.com/uploads/electricrocket/220994246997171/530936783722725956 3/IEPC-2022-102_HollowCathode_Daniel_Zschaetzsch.pdf.
[20] A. Gurciullo, A. Lucca Fabris, A. Knoll, Direct current plasma electron source for electric propulsion applications using atomic and molecular propellants, IEEE Trans. Plasma Sci. 45 (9) (2017) 2472–2480, http://dx.doi.org/10.1109/TPS.2017.2733345.
[21] H. Watanabe, et al., Performance evaluation of radio frequency plasma cathode for hall effect thruster, in: 34th International Electric Propulsion Conference, Hyogo-Kobe, 2015, URL http://electricrocket.org/IEPC/IEPC-2015-194_ISTS-2015-b-194.pdf.
[22] H. Watanabe, et al., Performance evaluation of TAL-type hall thruster with RF plasma cathode, in: 34th International Electric Propulsion Conference, Hyogo-Kobe, 2015, URL http://electricrocket.org/IEPC/IEPC-2015-217_ISTS-2015-b-217.pdf.
[23] K. St. Weis, et al., Development of a capacitively coupled insert-free RF-neutralizer, in: 29th International Electric Propulsion Conference, Princeton, USA, 2005, URL http://electricrocket.org/IEPC/086.pdf.
[24] F. Scholze, M. Tartz, H. Neumann, Inductive coupled radio frequency plasma bridge neutralizer, Rev. Sci. Instrum. 79 (2) (2008) 02B724, http://dx.doi.org/10.1063/1.2802587.
[25] S. Jahanbakhsh, M. Satir, M. Celik, Study of electron current extraction from a radio frequency plasma cathode designed as a neutralizer for ion source applications, Rev. Sci. Instrum. 87 (2) (2015) 02B922, http://dx.doi.org/10.1063/1.4935015.
[26] P. Dietz, F. Becker, K. Keil, K. Holste, P. Klar, Performance of a rf neutralizer operating with noble gases and iodine, Eur. Phys. J. Appl. Phys. 91 (1) (2020) 10901, http://dx.doi.org/10.1051/epjap/2020190213.
[27] H. Kamhawi, J. Foster, M. Patterson, Operation of a microwave electron cyclotron resonance cathode, in: 40th AIAA Joint Propulsion Conference, Fort Lauderdale, 2004, http://dx.doi.org/10.2514/6.2004-3819.
[28] H. Kamhawi, J. Foster, Investigation of various microwave electron cyclotron resonance cathode configurations, in: 29th International Electric Propulsion Conference, Princeton, 2005, URL http://electricrocket.org/IEPC/283.pdf.
[29] I. Funaki, H. Kuninaka, Overdense plasma production in a low-power microwave discharge electron source, Japan. J. Appl. Phys. 40 (Part 1, No. 4A) (2001) 2495–2500, http://dx.doi.org/10.1143/JJAP.40.2495.
[30] W. Ohmichi, H. Kuninaka, Performance degradation of a spacecraft electron cyclotron resonance neutralizer and its mitigation, J. Propuls. Power 30 (5) (2014) 1368–1372, http://dx.doi.org/10.2514/1.B35062.
[31] T. Morishita, R. Tsukizaki, K. Nishiyama, H. Kuninaka, Plasma parameters measured inside and outside a microwave-discharge-based plasma cathode using laser-induced fluorescence spectroscopy, J. Appl. Phys. 131 (1) (2022) 013301, http://dx.doi.org/10.1063/5.0071294.
[32] D. Lev, D. Pedrini, D. Goebel, et al., Recent progress in research and development of hollow cathodes for electric propulsion, Rev. Mod. Plasma Phys. 3 (6) (2019) http://dx.doi.org/10.1007/s41614-019-0026-0.
[33] K. Nishiyama, S. Hosoda, H. Kuninaka, Operational characteristics of a microwave discharge neutralizer for the ECR ion thruster μ20, in: 31st International Electric Propulsion Conference, Michigan, 2009, URL https://electricrocket.org/IEPC/IEPC-2009-021.pdf.
[34] H. Koizumi, H. Kuninaka, The application of 500 ma class microwave discharge neutralizer to hall thruster system of DubaiSat-2 satellite, in: Proceedings of Space Transportation Symposium: FY2012, 2013, URL http://id.nii.ac.jp/1696/00016298/.
[35] N. Bradbury, Electron attachment and negative ion formation in oxygen and oxygen mixtures, Phys. Rev. 44 (1933) 883–890, http://dx.doi.org/10.1103/PhysRev.44.883.
[36] A. Taploo, L. Lin, M. Keidar, Analysis of ionization in air-breathing plasma thruster, Phys. Plasmas 28 (9) (2021) http://dx.doi.org/10.1063/5.0059896.
[37] M. Tisaev, B. Karadag, E. Ferrato, A. Kitaeva, T. Andreussi, A. Lucca Fabris, Development of an air-breathing neutraliser as part of the aether system, in: 37th International Electric Propulsion Conference, Cambridge, USA, 2022, URL https://www.jotform.com/uploads/electricrocket/220994246997171/531532138553165877 6/IEPC22_105_Neutraliser_development.pdf.
[38] M. Tisaev, B. Karadag, A. Lucca Fabris, Influence of applied magnetic field in an air-breathing microwave plasma cathode, J. Phys. D: Appl. Phys. 56 (46) (2023) 465203, http://dx.doi.org/10.1088/1361-6463/acefe2.
[39] Stainless steel-austenitic-1.4301 (304) data sheet, 2023, URL https://www.aalco.co.uk/datasheets/Stainless-Steel-14301-304-Bar-and-Section_34.ashx.
[40] C. Balanis, Antenna Theory - Analysis and Design, fourth ed., John Wiley & Sons, 2016.
[41] D. Gray, American Institute of Physics Handbook (9J: Work Function and Secondary Emission), third ed., McGraw-Hill, 1972.
[42] M. Lieberman, A. Lichtenberg, Principles of Plasma Discharges and Materials Processing, second ed., John Wiley & Sons, 2005.
[43] P. Brix, G. Herzberg, The dissociation energy of oxygen, J. Chem. Phys. 21 (12) (1953) 2240, http://dx.doi.org/10.1063/1.1698843.
[44] D. Frost, C. McDowell, The dissociation energy of the nitrogen molecule, Proc. R. Soc. London. Math. Phys. Sci. 236 (1205) (1956) 278–284, http://dx.doi.org/10.1098/rspa.1956.0135.
[45] D. Frost, C. McDowell, The ionization and dissociation of oxygen by electron impact, J. Am. Chem. Soc. 80 (23) (1958) 6183–6187, http://dx.doi.org/10.1021/ja01556a009.
[46] D. Frost, C. McDowell, Studies of the ionization of molecules by electron impact. I. Excited states of the nitrogen molecular ion, Proc. R. Soc. London. Ser. A, Math. Phys. Sci. 232 (1189) (1955) 227–235, URL http://www.jstor.org/stable/99762.
[47] Basic Atomic Spectroscopic Data: O, National Institute of Standards and Technology, 2023, URL https://physics.nist.gov/PhysRefData/Handbook/Tables/oxygentable1.htm.
[48] Basic Atomic Spectroscopic Data: N, National Institute of Standards and Technology, 2023, URL https://physics.nist.gov/PhysRefData/Handbook/Tables/nitrogentable1.htm.
[49] S. Walton, J. Tucek, R. Champion, Y. Wang, Low energy, ion-induced electron and ion emission from stainless steel: The effect of oxygen coverage and the implications for discharge modeling, J. Appl. Phys. 85 (3) (1999) 1832–1837, http://dx.doi.org/10.1063/1.369330.
[50] D. Ruzic, R. Moore, D. Manos, S. Cohen, Secondary electron yields of carbon-coated and polished stainless steel, J. Vac. Sci. Technol. 20 (4) (1982) 1313–1316, http://dx.doi.org/10.1116/1.571569.
[51] E. Oyarzabal, A. Martín-Rojo, J. Ferreira, D. Tafalla, F. Tabarés, Anomalous secondary electron emission of metallic surfaces exposed to a glow discharge plasma, J. Nucl. Mater. 438 (2013) S792–S795, http://dx.doi.org/10.1016/j.jnucmat.2013.01.170, Proceedings of the 20th International Conference on Plasma-Surface Interactions in Controlled Fusion Devices.
[52] E. Oyarzabal, A. Martin-Rojo, F. Tabarés, Electron-induced secondary electron emission coefficient of lithium, tungsten and stainless steel surfaces exposed to low-pressure plasmas, J. Nucl. Mater. 452 (1) (2014) 37–40, http://dx.doi.org/10.1016/j.jnucmat.2014.04.046.
[53] M. Konuma, Film Deposition by Plasma Techniques, First, Springer Berlin, 1992.
[54] V. Lisovskiy, V. Yegorenkov, Alpha–gamma transition in RF capacitive discharge in low-pressure oxygen, Vacuum 74 (1) (2004) 19–28, http://dx.doi.org/10.1016/j.vacuum.2003.11.003.
[55] N. Matsunami, et al., Energy dependence of the ion-induced sputtering yields of monatomic solids, At. Data Nucl. Data Tables 31 (1) (1984) 1–80, http://dx.doi.org/10.1016/0092-640X(84)90016-0.
[56] A. Martinez-Garcia, et al., High rate and durable, binder free anode based on silicon loaded moo3 nanoplatelets, Sci. Rep. 5 (2015) http://dx.doi.org/10.1038/srep10530.
[57] Y. Itikawa, A. Ichimura, Cross sections for collisions of electrons and photons with atomic oxygen, J. Phys. Chem. Ref. Data 19 (3) (1990) 637–651, http://dx.doi.org/10.1063/1.555857.
[58] E. Brook, M. Harrison, A. Smith, Measurements of the electron impact ionisation cross sections of He, C, O and N atoms, J. Phys. B: At. Mol. Phys. 11 (17) (1978) 3115, http://dx.doi.org/10.1088/0022-3700/11/17/021.
[59] D. Rapp, P. Englander-Golden, Total cross sections for ionization and attachment in gases by electron impact. I. Positive ionization, J. Chem. Phys. 43 (5) (1965) 1464–1479, http://dx.doi.org/10.1063/1.1696957.
[60] T. Morishita, R. Tsukizaki, S. Morita, D. Koda, K. Nishiyama, H. Kuninaka, Effect of nozzle magnetic field on microwave discharge cathode performance, Acta Astronaut. 165 (2019) 25–31, http://dx.doi.org/10.1016/j.actaastro.2019.08.025.